nature communications

Article

https://doi.org/10.1038/s41467-024-53729-w

Multiplexed expansion revealing for imaging multiprotein nanostructures in healthy and diseased brain

Received: 9 September 2023

Accepted: 21 October 2024

Published online: 09 November 2024

Check for updates

Jinyoung Kang[1,2,14], Margaret E. Schroeder[1,3,14], Youngmi Lee[1], Chaitanya Kapoor[4], Eunah Yu[1], Tyler B. Tarr[5], Kat Titterton[1], Menglong Zeng[1], Demian Park[1], Emily Niederst[6], Donglai Wei[7], Guoping Feng[1,2,3,8] & Edward S. Boyden[1,2,3,9,10,11,12,13]

Proteins work together in nanostructures in many physiological contexts and disease states. We recently developed expansion revealing (ExR), which expands proteins away from each other, in order to support better labeling with antibody tags and nanoscale imaging on conventional microscopes. Here, we report multiplexed expansion revealing (multiExR), which enables high-fidelity antibody visualization of >20 proteins in the same specimen, over serial rounds of staining and imaging. Across all datasets examined, multiExR exhibits a median round-to-round registration error of 39 nm, with a median registration error of 25 nm when the most stringent form of the protocol is used. We precisely map 23 proteins in the brain of 5xFAD Alzheimer's model mice, and find reductions in synaptic protein cluster volume, and co-localization of specific AMPA receptor subunits with amyloid-beta nanoclusters. We visualize 20 synaptic proteins in specimens of mouse primary somatosensory cortex. multiExR may be of broad use in analyzing how different kinds of protein are organized amidst normal and pathological processes in biology.

A single cell contains perhaps thousands of kinds of protein, which interact over nanoscale distances with each other to mediate biological processes. Disturbing that arrangement can corrupt signaling, and lead to pathological states[1]. Ideally one would be able to map the location, and identity, of many proteins within the same preserved cell or tissue specimen, with nanoscale precision. Such a map could generate novel hypotheses, and even insights, into how proteins might interact with each other, in a healthy or diseased state. However, studying proteins in their system contexts is complex, due to their nanoscale size, and the crowded nature of their biological environment. Expansion microscopy is a form of light microscopy that benefits from physical expansion of specimens, via chemical introduction of a densely permeating swellable hydrogel throughout a biological sample. Biomolecules or labels of interest are covalently anchored to the hydrogel. The specimen is then chemically softened, and then water is added, causing the hydrogel-specimen composite to swell in an even fashion (typically 4x, although more recent protocols support 10x and 20x, and iterating the 4x procedure can also yield 20x). The

[1]McGovern Institute for Brain Research, MIT, Cambridge, MA, USA. [2]Yang Tan Collective, MIT, Cambridge, MA, USA. [3]Department of Brain and Cognitive Sciences, MIT, Cambridge, MA, USA. [4]Department of Electrical and Electronics Engineering, BITS Pilani, Rajasthan, India. [5]Department of Neuroscience, University of Pittsburgh, Pittsburgh, PA, USA. [6]The Picower Institute for Learning and Memory, MIT, Cambridge, MA, USA. [7]Department of Computer Science, Boston College, Chestnut Hill, MA, USA. [8]Broad Institute of MIT and Harvard, Cambridge, MA, USA. [9]Center for Neurobiological Engineering and K. Lisa Yang Center for Bionics, MIT, Cambridge, MA, USA. [10]Department of Biological Engineering, MIT, Cambridge, MA, USA. [11]Koch Institute, MIT, Cambridge, MA, USA. [12]Howard Hughes Medical Institute, Cambridge, MA, USA. [13]Media Arts and Sciences, MIT, Cambridge, MA, USA. [14]These authors contributed equally: Jinyoung Kang, Margaret E. Schroeder. e-mail: edboyden@mit.edu

https://doi.org/10.1038/s41467-024-53729-w

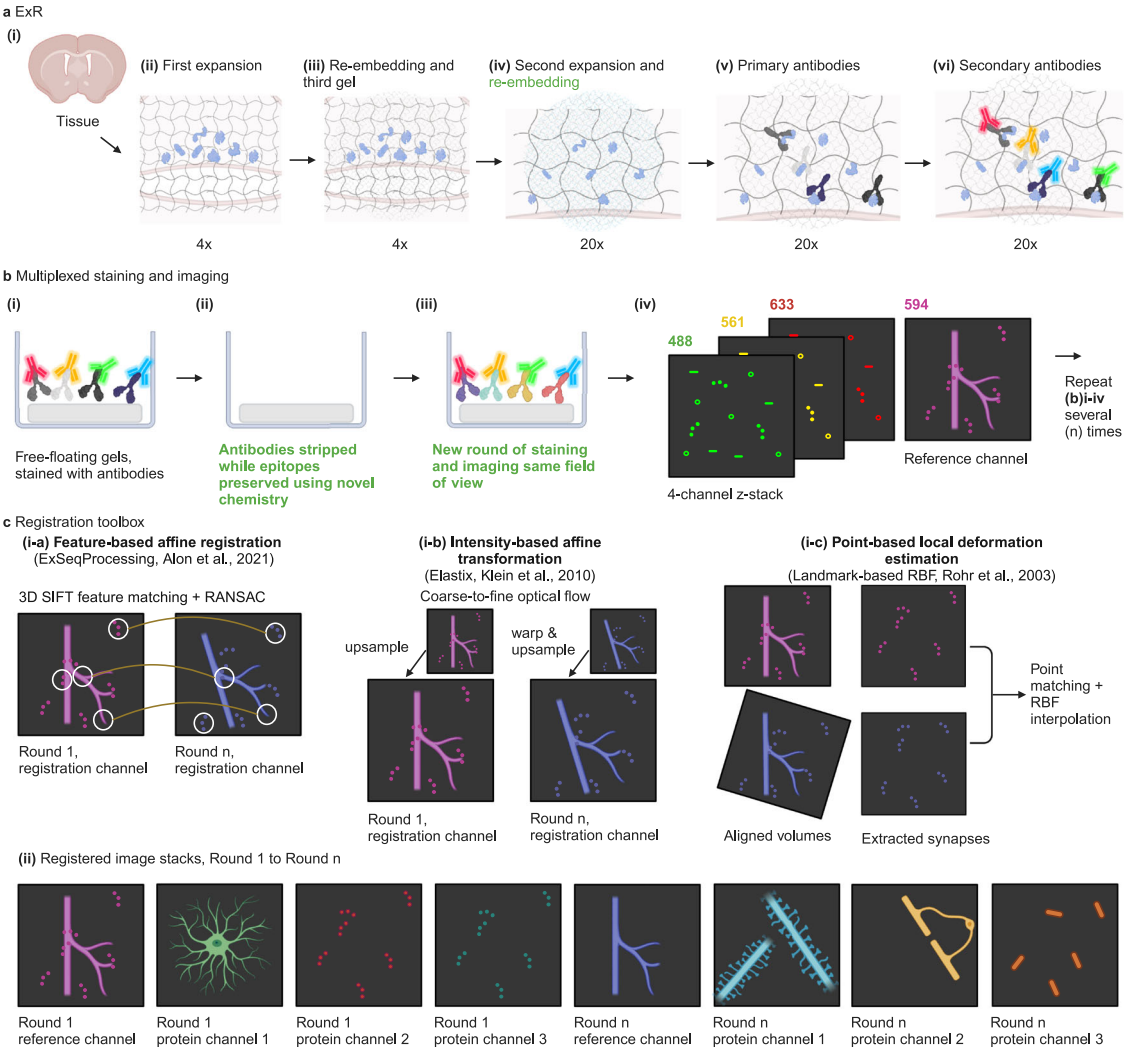

Fig. 1 | Schematic of multiExR procedure. a Expansion revealing (ExR), a technology for decrowding of proteins through isotropic protein separation. **a**i Coronal section of mouse brain before staining or expansion. **a**ii Anchoring and first gelation step. The specimen is embedded in a swellable hydrogel (gray wavy lines), mechanically softened via detergent and heat treatment, and expanded in water. **a**iii Re-embedding and second swellable gel formation. The fully expanded first gel is re-embedded in a charge-neutral gel (not shown), followed by the formation of a second swellable hydrogel (light gray wavy lines). **a**iv Final up to 20x expansion with the addition of water, followed by a recommended re-embedding step to preserve gel strength for multi-round imaging (blue wavy lines). **a**v, Post-expansion primary antibody staining (Y-shaped proteins). **a**vi Post-expansion staining with fluorescent secondary antibodies to visualize decrowded biomolecules. **b** Multiplexed ExR procedure. **b**i Free-floating gels are stained with conventional primary and secondary antibodies, and the images are collected. **b**ii After imaging, primary and secondary antibodies are stripped using detergent and heat-based denaturation while endogenous proteins are preserved by physical anchoring in hydrogel networks. **b**iii Gels are re-incubated with a new round of primary and secondary antibodies, and the same field of view is imaged again. **b**iv A 3 or 4-channel z-stack is obtained on a confocal microscope. One or more of the four channels serves as the reference channel. After imaging, the antibody stripping and staining processes are repeated for up to 10 rounds. **c** Registration of multi-round images using the reference channel. The multi-round images are registered using one or a combination of the methods (i-**a** and i-**c**, or i-**b** and i-**c**) in this toolbox (see Supplementary Fig. 1 and "Methods" section for more details). i-**a** a feature-based affine registration algorithm[8,9]. i-**b** an intensity-based affine registration algorithm[10] iteratively refining the estimation from the coarse scale of the image pairs to the fine scale. i-**c**, a point-based registration algorithm[11], designed specifically to further align fine structures. **c**ii Registered multiExR images are obtained after applying calculated warps to all channels from later rounds, creating multi-channel image volumes. Schematic created with BioRender.com. Bolded, green text highlights technical innovations of the multiExR procedure.

net effect is that the light microscope has an effectively increased resolution, even beating the diffraction limit[2].

Early forms of expansion microscopy focused on labeling biomolecules before expansion[3]. Recently, forms of expansion microscopy such as expansion revealing (ExR[4], Fig. 1a), which pulls proteins apart from each other throughout a specimen via a process of specimen hydrogel embedding, protein anchoring to the hydrogel, epitope-preserving specimen softening, and isotropic sample swelling, have begun to enable densely packed proteins to be separated from one another. Separated proteins can be more easily stained by labels, given the better access supported. Thus, proteins previously invisible in light microscopy can become visible. ExR, which expands samples by ~20x in linear dimension, supports ~20 nm resolution imaging on ordinary microscopes. To date, ExR has been used to visualize a few proteins at once within a specimen, limited by the spectral properties of the fluorophores used. Many different hardware platforms have been proposed for the purposes of improving the number of biomolecules visualizable within a specimen[5–7], but most of these are not commonly available in ordinary biology laboratories. Techniques like ExM have become popular in part because they do not require novel hardware to be purchased by a biology group, which has led to rapid adoption in everyday biology experiments[3]. We thus asked whether it would be

possible to devise a multiplexed form of ExR that could enable the imaging of potentially arbitrary numbers of proteins, with nanoscale precision, in the same expanded specimen, without requiring hardware not commonly available in biology labs.

We here describe a multiplexed form of ExR (multiExR), which extends ExR through serial rounds of post-expansion staining, imaging, and washing. We optimized and validated each chemical step of this process, enabling ~20 proteins in the same tissue sample to be visualized, using conventional antibodies, with low signal deterioration or bleed-through between rounds. Due to the mechanical properties of expanded gels, precise registration of these images across rounds posed a challenge. We optimized experimental conditions, and building from prior work[8], implemented registration algorithms to register serial imaging rounds with high precision. In the most stringent form of the protocol (Supplementary Fig. 1Bii, path 2 in Supplementary Fig. 1A), which we applied to our primary validation dataset, we achieved a median (taken across all staining round pairs for all fields of view, i.e. each combination of round pair and field of view was considered as one sample) round-to-round registration error of 25 nm (minimum 14 to maximum 98 nm). The staining and registration steps can be tuned to trade off between precision and throughput, as prioritized by the user. We do not recommend the aforementioned stringent form for beginners, because it is laborious: if such high precision is not required, the process can be conducted more quickly, albeit at the cost that the round-to-round alignment error could rise to 100 nm or more.

We demonstrated that multiExR, used with 23 different antibodies against different proteins, could be used to characterize known, and previously undescribed, pathology, revealing nanoscale colocalizations between multiple synaptic proteins and amyloid-beta (Aβ) nanoclusters in the 5xFAD Alzheimer's model mouse brain. We also visualized putative synapses, imaging 20 proteins in the same specimen, in the mouse somatosensory cortex. Thus, multiExR offers great utility in the mapping of protein organization in healthy and disease states, potentially yielding novel hypotheses of molecular mechanism and/or drug target, and perhaps even someday diagnostics, in biology and medicine.

Results

Optimizing ExR for multi-round staining, imaging, and registration

The approach for multiExR is schematized in Fig. 1. Tissue and gel preparation are identical to those of ExR, until after the final expansion step, when an additional re-embedding step is performed to increase gel density and strength (Fig. 1a). One channel serves as a reference channel to enable registration across imaging rounds. For most of the datasets presented here, we used three different molecular targets, all labeled with the same fluorophore, to provide a reference channel that exhibits features ranging from the nanoscale to the macroscale, so that accurate registration is possible both at the scale of the entire specimen, as well as at the nanoscale. Criteria for a protein (or set of proteins) to be chosen as a reference include high signal-to-noise ratio and adequate feature density. It may also be useful to choose a reference protein with some structural, morphological, or cell type information that guides the viewer to appropriate subvolumes for detailed imaging. In the current study, we primarily use Lycopersicon Esculentum Lectin combined with glial fibrillary acidic protein (GFAP) and neurofilament (SMI) and sometimes the synaptic scaffold Homer1, with all molecules being labeled with the same color fluorophore, as a reference channel. The multi-scale nature of our reference channel is important, since a reference channel with only macroscale features lacks the information to support registration with nanoprecision, and a reference channel with only nanoscale features is difficult to align at the macroscale.

During imaging, we searched for fields of view with high feature density in the reference channel, to ensure adequate feature density in the reference channel used to support alignment, for each field of view. More specifically, we found that a reference channel feature density of ~1.3% (Supplementary Table 1), with both large (e.g., largest feature ~50% of total reference feature volume like Lectin, Supplementary Table 1) and small (e.g., smallest features 2.832^{-3}% of total reference feature volume like synaptic proteins, Supplementary Table 1) features present (Supplementary Fig. 2a), was sufficient for accurate registration across rounds with median round-to-round precision of 25 nm across all staining round pairs for all fields of view, in the most stringent form of the protocol (Supplementary Fig. 1Bii). Here, and throughout the paper, unless otherwise indicated, this median was calculated as follows: first, registration errors were averaged across ~1,000 randomly sampled subvolumes within each field of view. Then, those averages were analyzed across round pairs (e.g., rounds 1–2, 1–3, 1–4, etc.) for all fields of view, and the median taken across all round pairs and fields of view. We calculated feature density as the fraction of total image volume occupied by feature volume in the reference channel, which is the normalized sum of all channels in that round in Fig. 2, but in other datasets is the three-target channel described above. The staining, imaging, and registration steps can be relaxed in stringency if such precision is not needed, but greater throughput is valued, resulting in a version of the protocol that offers usually <100 nm, but occasionally higher, round-to-round precision (see Supplementary Fig. 1 for flowchart to help users choose the optimal protocol for a given scientific question). We recommend this relaxed-stringency protocol for beginners, due to its simpler nature.

Following the first round of imaging, antibodies are stripped using an ExR-optimized protocol. 100 mM beta-mercaptoethanol-containing denaturation buffer (200 mM sodium dodecyl sulfate (SDS), 200 mM NaCl, and 50 mM Tris pH 9), which can break antibody disulfide bonds and support protein denaturation with minimal heat treatment, was used to remove antibody stains post-imaging (Fig. 1b, see "Methods" section for details). These stripping conditions were optimal for preserving anchored epitopes while minimizing signal carryover between staining rounds, as shown below. The next round of staining, imaging, and stripping is then performed, iterating as needed. The reference channel, which in most of the datasets presented here was composed of three or more different molecular targets (Supplementary Fig. 1), is used to locate the same field of view in each imaging round, and to align the images across rounds, as described in the next paragraph. Importantly, to minimize gel drift, for successful downstream registration, we found it necessary to stabilize gels before taking images, by removing the buffer around gels as much as possible, and placing a sealing film over the well plate containing the gel to avoid gel drying during imaging.

Computational registration with nanoscale precision of multiExR images taken across multiple rounds of staining and imaging initially posed great difficulty, despite innovations such as our multiscale reference stain, and the aforementioned improvements in sample stabilization. multiExR gels are free-floating, because immobilization of gels used in standard ExM imaging reduces antibody stripping efficiency (and gels would often detach from glass surfaces during antibody stripping). However, free-floating gels exhibit more degrees of freedom, and thus variability, between rounds of imaging than immobilized gels. Furthermore, due to the highly expanded nature of ExR gels, and the dilution of tissue structure due to such expansion, features can be sparser than ideal for registration. Finally, slight variation in signal-to-noise ratio (SNR), perhaps due to the stochasticity of antibody binding visible at the nanometer scale, means that even identical staining and imaging conditions across rounds can lead to slightly, but significantly, different images in the reference channel – perhaps a fundamental issue for any nanoimaging protocol involving antibody staining. For these reasons, multiExR registration cannot be accomplished with conventional intensity-based methods optimized

https://doi.org/10.1038/s41467-024-53729-w

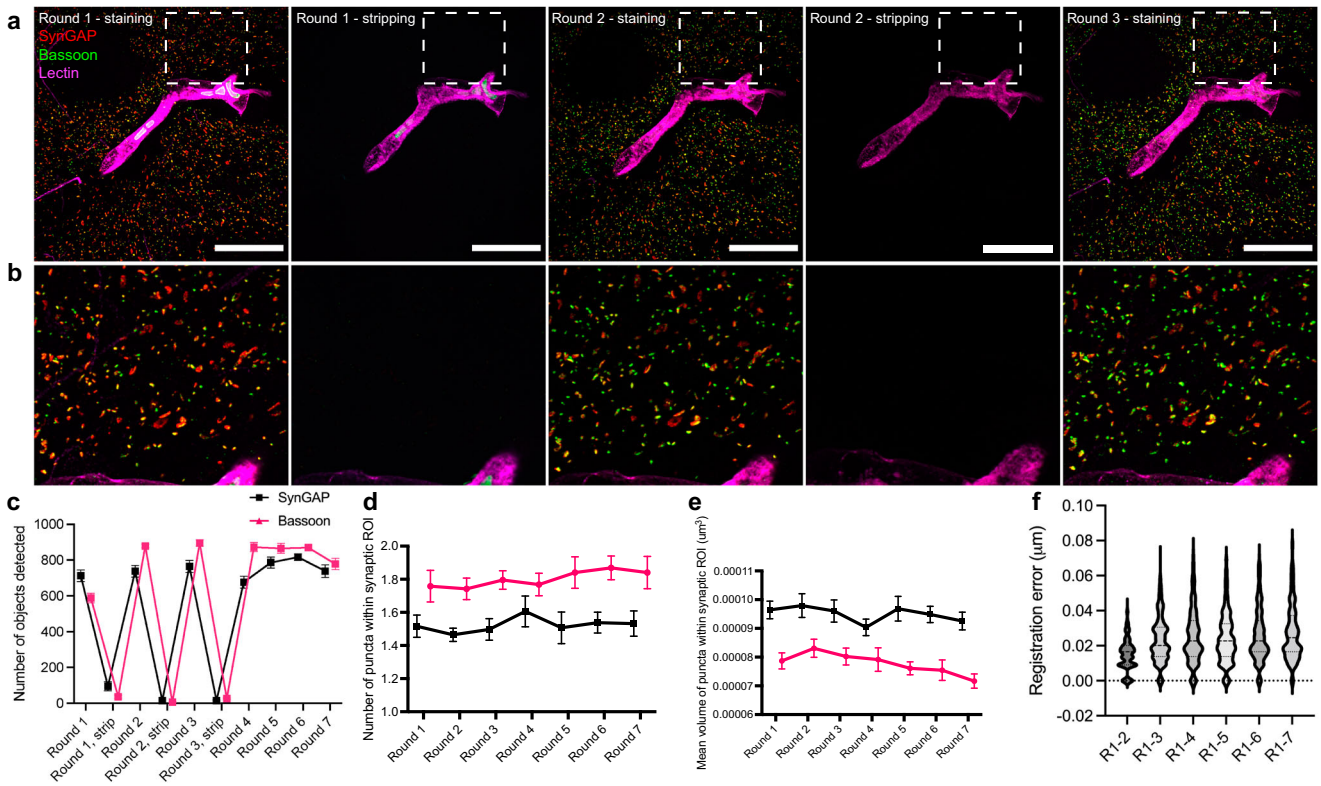

Fig. 2 | Validation of multiExR technology by staining, stripping, and re-staining the same set of primary and secondary antibodies across multiple rounds in the mouse somatosensory cortex. a Example field of view (max intensity projection) of registered validation dataset images in round 1, stripping after round 1, round 2, stripping after round 2, and round 3. Pixel intensities are adjusted to the same minimum and maximum values for staining and stripping rounds. **b** Zoom in of boxed region of (**a**). Scale bar, 5 µm in biological units (i.e., real size divided by expansion factor). **c** Mean number of objects detected in a field of view (see "Methods" section) after 7 staining rounds and the first 3 stripping rounds ($n = 7$ fields of view from one mouse for staining rounds, where the first 3 stripping rounds were imaged but stripping was performed between all rounds). **d** Mean number of puncta detected in manually-identified synaptic regions of interest (ROIs) after 7 staining rounds (the same $n = 7$ fields of view from one mouse, mean is taken over 51-53 ROIs per field of view). **e** Mean volume of puncta detected in manually-identified synaptic ROIs after 7 staining rounds (the same $n = 7$ fields of view from one mouse, mean is taken over 51-53 ROIs per field of view). Error bars in **c**–**e** represent standard error of the mean across the fields of view. **f** Estimated population distribution (violin plot of density, with a dashed line at the median and dotted lines at the quartiles) of the registration error in a representative field of view (different from panels (**a**, **b**), as it was more representative of registration error). The 95% confidence interval for each round pair is [0.01467, 0.01578] for rounds 1–2, [0.02271, 0.02430] for rounds 1–3, [0.02443, 0.02635] for rounds 1–4, [0.02337, 0.02516] for rounds 1–5, [0.02491, 0.02881] for rounds 1–6, and [0.02657, 0.02855] for rounds 1–7 (see "Methods" section, $n = 1000$ randomly sampled subvolumes from one field of view from one mouse). Source data are provided as a Source Data file.

for fixed, unexpanded tissue images, such as those in popular Fiji plugins.

To address this challenge, we created a toolbox for both global and local alignment of multiExR imaging rounds, consisting of: a 3D scale-intensity feature transform (SIFT)-based global registration algorithm adapted from previous algorithms for multiround alignment of multiplexed RNA ExM images (ExSeqProcessing registration[8,9]), an alternative intensity-based global registration algorithm[10], and an optional point-based alignment step for refinement of local structures such as synapses[11] (Fig. 1c, see "Methods" section for details). Users can choose between the two global algorithms, and whether to add a local registration step, based on the signal-to-noise ratio of their images (see Supplementary Fig. 1 for a flowchart of how to choose the experimental and computational workflow depending on desired goal). If it is necessary to register small, punctate objects such as synapses to one another, with high accuracy, across subsequent rounds, the point-based alignment algorithm can improve local registration accuracy.

We recommend starting with the feature-based ExSeqProcessing registration algorithm, as we found this could accurately and reliably align multiExR imaging rounds for most of our datasets within 100 nm (median 43 nm, minimum 6.2 nm, maximum 151 nm) and has a fast runtime of <30 minutes per field of view when implemented with graphic processing unit (GPU) acceleration. Users can quickly evaluate registration quality by examining composite overlays of the reference channel between different imaging rounds in Fiji: micron-scale registration errors will be evident by a lack of colocalized signal. Nanoscale registration errors can be quantified in a few hours using the pipeline described in the "Methods" section.

We quantitatively validated multiExR signal, background, and registration error, by staining for the same target synaptic proteins (SynGAP and Bassoon) repeatedly over seven rounds of staining, imaging, and stripping, using the same microscope settings. In general, the absolute intensity of an immunostained protein can be highly variable and depends on many experimental factors, some of which are controllable and some of which are not. Therefore, we do not claim that absolute intensity is constant over multiple rounds of stripping and staining with multiExR. Instead, we focus on measures of volume, signal-to-noise, intensity ratio, and number of detectable objects – more robust metrics – in the following analyses.

To confirm stripping efficacy, we stained only with Lectin after stripping antibodies, to find the same field of view, then obtained images using the same laser power and exposure time, finding that there was minimal residual signal, which in turn would lead to negligible bleed-through between rounds (Fig. 2a, b and Supplementary Fig. 2). Later rounds maintained high SNR for target synaptic proteins, evidenced by cross-round stability in the number of detected objects

in the whole field of view (putative synapses, Fig. 2c and Supplementary Fig. 2a), the SNR of specific synaptic proteins within manually-identified putative synapses (Supplementary Fig. 2b), the number of protein puncta within these putative synapses (Fig. 2d) and the volume of these puncta (Fig. 2e). We note that the last three of these measures compare the SNR and number of puncta within identified putative synapses, relevant to the building up of information about a given synapse over many rounds of protein identification and localization. We note persistent Bassoon staining on the blood vessel after stripping round 1, but not after stripping round 2. We speculate that insufficient stripping may be more likely to occur for "stickier" structures like blood vessels, where there may be more non-specific binding of Fc fragments, as we did not observe insufficient stripping outside of blood vessels. We observed non-specific staining in blood vessels, for some proteins, in all datasets (Figs. 3a, b and 5a and Supplementary Figs. 3a and 6).

We observed that the Bassoon signal intensity, relative to SynGAP, increased markedly after the first round of stripping, and remained stable in subsequent rounds (Fig. 2a, b). To quantify this increase, we calculated the mean signal intensity (in background subtracted images) of pixels in synaptic puncta within manually-identified synaptic regions of interest (ROIs) and found this to be increased in the second and third staining rounds (Supplementary Fig. 2ci), consistent with an antigen retrieval-like effect following the harsh denaturation conditions used in antibody stripping, that affects the Bassoon but not SynGAP target epitope. In contrast, the absolute intensity of SynGAP staining, and of Bassoon staining on rounds beyond the third round, decreased somewhat steadily with successive rounds of stripping and re-staining (Supplementary Fig. 2cii), which suggests a general process of epitope staining efficacy decline occurs during harsh stripping conditions. However, the signal-to-noise ratio, number of puncta and puncta volumes (Fig. 2d, e and Supplementary Fig. 2b) were stable across rounds, demonstrating that while absolute intensity may vary between rounds of staining, detection of biologically meaningful objects was maintained. In particular, it is striking that although absolute signal drops by a factor of 2 or 3, signal-to-noise (computed as signal of the object divided by signal of the background) stays constant – meaning that changes in epitope staining efficacy may apply equally to background staining as to object staining, consistent with other work[12]. However, not all epitopes increase staining after stripping treatment; some decrease in brightness (Supplementary Fig. 2c). Thus, the cost and benefit of stripping-based antigen retrieval will need to be evaluated on a target-by-target basis, in pilot experiments, to gauge whether to pursue it deliberately or not, before staining.

To assess whether the stripping process affected the reference channel, we measured the mean signal intensity of the maximum intensity projection of the registered Lectin channel for each field of view and each staining and stripping round, in which the reference channel was re-stained to locate the same field of view as in the previous round. While the mean signal intensity in the single-channel Lectin reference channel did decline somewhat after the first round (Supplementary Fig. 2d and Supplementary Table 3i), the magnitude of the mean signal intensity was relatively stable in later rounds. Taken with the SynGAP and Bassoon findings, this result highlights that antigen retrieval effects may not only boost intensity, but may sometimes suppress intensity. While there was significant variation in mean signal intensity between the rounds, there was no systematic pattern to the variation (Supplementary Table 3ii–iii). Given that decreases in intensity are possible with multiExR, it is possible that multiExR will not be ideal in situations where signals are very weak, or single molecule counting is required; given that one key advantage of ExR is the decrowding of densely packed, concentrated protein clusters, for better labeling, this may be a moot point. Nevertheless, even in the stripping rounds, where only the Lectin channel was re-stained (Supplementary Fig. 1B(iii), same as reference channel strategy **1(iii)**, using registration algorithm **2(i)**), there remained sufficient signal to register the images within 80 nm on average, and often within 50 nm on average (Supplementary Table 2). Thus, regardless of the magnitude of signal intensity in the reference channel, its functional integrity is maintained after stripping, to an extent sufficient to make meaningful conclusions and to align images.

For this first validation dataset, we utilized 4 single-protein channels combined (normalized and summed) to a single reference channel (path 7, reference channel option **1(ii)** in Supplementary Fig. 1, omitting registration algorithm **2(iii)**). The median registration error across all staining round pairs for all fields of view, calculated as previously described[8], using the SynGAP channel, was 25 nm (i.e., 2–3 pixels for the microscope settings used), with consistent performance for most round pairs: 71.4% exhibited registration error <30 nm (Fig. 2f, see Supplementary Table 2 for full statistics).

In a second validation experiment (Supplementary Fig. 3), we used 4 proteins (Lectin, neurofilament SMI, GFAP, and Homer) in a single reference channel for registration (path 9, reference channel option **1(i)** in Supplementary Fig. 1), similar to what we used in many later experiments (Figs. 3–5**)**, to increase the number of target proteins that can be imaged per round. Four round pairs that had poor or failed registration using the global feature-based registration algorithm (**2(i)** in Supplementary Fig. 1c) were registered using the global intensity-based algorithm (**2(ii)** in Supplementary Fig. 1c). The median registration error, calculated as described above using the reference channel, was 66 nm, with consistent performance for most staining round pairs (59.3% of staining round pairs for all fields of view exhibited mean (across subvolumes) registration error <70 nm) in most fields of view, and all but one round pair across all fields of view had mean (across subvolumes) registration error <100 nm in staining rounds (Supplementary Fig. 3b, see Supplementary Table 4 for full statistics). We speculate that the higher registration error in this secondary validation dataset was due to signal intensity differences between the proteins co-stained in the single reference channel (Supplementary Fig. 3a), which reduced the quality of feature detection across scales during SIFT-based registration. The registration accuracy obtained from rounds using the global intensity-based algorithm, which was only used when the SIFT-based algorithm failed, was similar to that of the other rounds (Supplementary Table 4).

Seven rounds of multiExR could reveal 21 different biomolecules, if three target proteins were imaged per round, with the fourth color reserved for the reference channel. We demonstrate at least 20 proteins in the same field of view, in the examples in the rest of this paper. To our knowledge, this is the highest number of different biomolecules visualized in the same tissue specimen with such nanoscale spatial precision. In principle, 20-protein multiExR could reveal 20 ×19 / 2 = 190 different protein-protein relationships.

Nanoscale multiplexed characterization of amyloid beta and synapse pathology in Alzheimer's model mouse brain

To demonstrate the utility of multiExR for profiling multiplexed protein configurations, we explored the nanoscale organization of 23 proteins in 12-month-old Alzheimer's model 5xFAD[13] and age-matched wild-type (WT) mouse brains (12-13 months of age; Fig. 3a, b and Supplementary Table 5). We chose to characterize three amyloid-beta species with antibodies: 12F4[14], which targets the C-terminus of Aβ−42; D54D2, which targets several isoforms of human Aβ (Aβ−37, Aβ−38, Aβ−39, Aβ−40, and Aβ−42); and 6E10, which targets amino acid residues 1-16 of human Aβ, to see how their staining patterns differed, with nanoscale precision. For registration across rounds, we used registration channel option **1(i)** and registration algorithm **2(i)** from Supplementary Fig. 1C. Images were obtained from 8 fields of view from 2 WT mice and 9 fields of view from 2 5xFAD mice. We achieved a median registration error of 34 nm across all fields of view and all round pairs (Supplementary Table 6).

https://doi.org/10.1038/s41467-024-53729-w

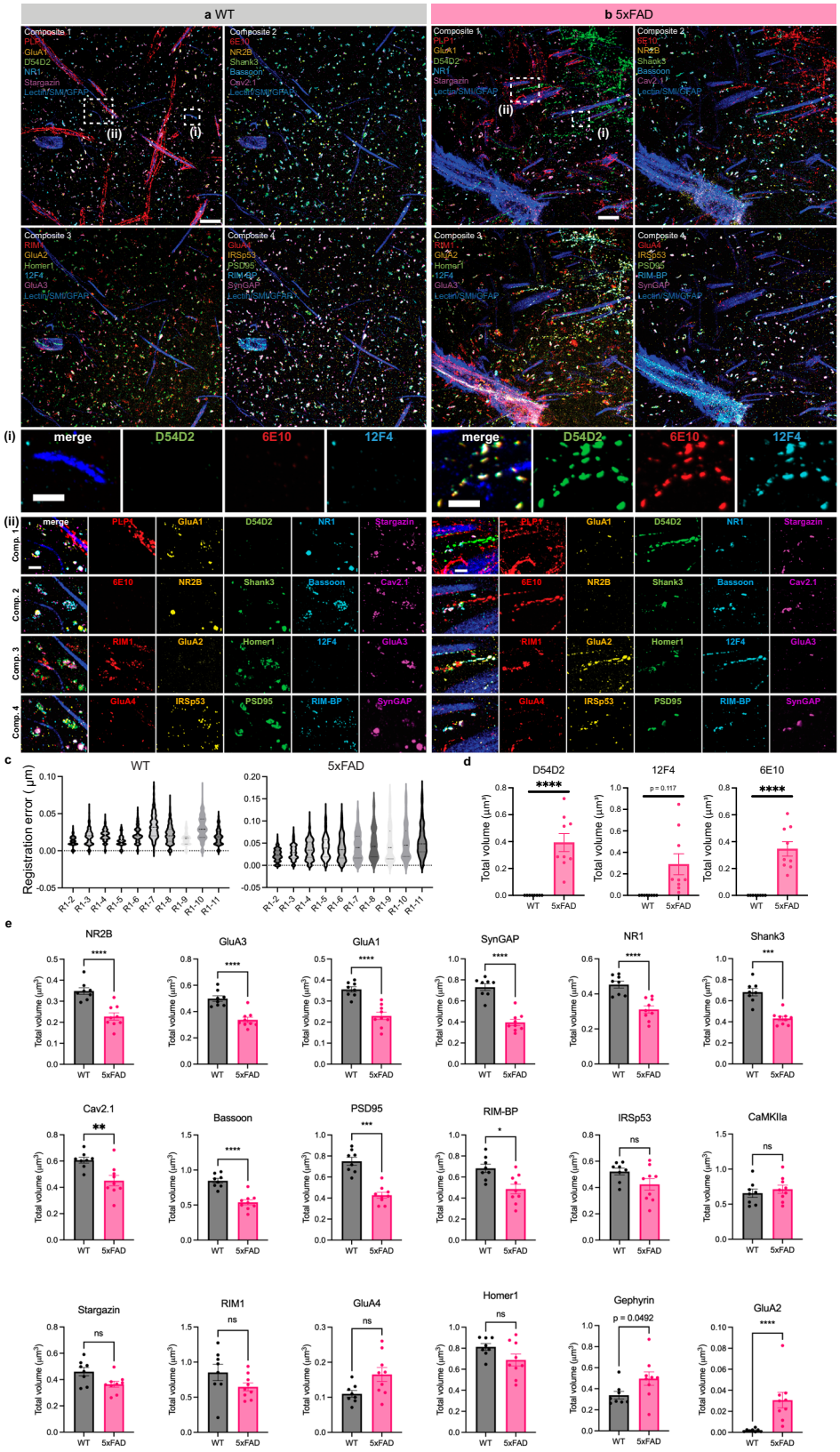

As expected, we observed increased amyloid beta burden as measured by the total volume of intensity-thresholded regions in the cortex of 5xFAD brains as compared to WT for D54D2 and 6E10 (Fig. 3d). The difference in volume for D54D2 and 6E10 reached statistical significance (linear mixed effect model accounting for multiple observations per animal, p-value on group effect = 1.19×10^{-5} for D54D2, 0.117 for 12F4, and 1.50×10^{-8} for 6E10). We then leveraged multiplexing to examine synapse alterations, a hallmark of Alzheimer's disease pathology that precedes cognitive decline[15], at nanoscale resolution. We first wondered whether Aβ nanodomains might preferentially colocalize with specific synaptic proteins in 5xFAD brains (Fig. 3bii), and proceeded to analyze the data in several steps. First, we

Fig. 3 | 23-plex nanoscale characterization of amyloid beta pathology and synapse loss in Alzheimer's model mouse somatosensory cortex. a, **b** 6-channel and composite maximum intensity projections of Aβ and synaptic proteins in representative fields of view and zoom-ins (lower panels) from WT (**a**) and 5xFAD (**b**), obtained using multiExR. Scale bar, 2 μm (upper panels), (i) and (ii) 500 nm. **c** Violin plots of the population distribution of registration error for these fields of view. **d** Total volume in intensity-thresholded regions (see Methods) for D54D2, 12F4, and 6E10 Aβ species in WT and 5xFAD registered fields of view (statistical significance determined using a linear mixed effects model without multiple comparisons correction, $n = 17$ fields of view from two WT and two 5xFAD animals, error bars are mean ± standard error of the mean. **e** Total volume of objects detected after intensity thresholding and size filtration in WT and 5xFAD registered fields of view (statistical significance determined using a linear mixed effects model without multiple comparisons correction, the same $n = 17$ fields of view from two WT and two 5xFAD animals, error bars are mean ± standard error of the mean) for various synaptic proteins (see Supplementary Table 7 for full statistics). WT wild type, 5xFAD 5x familial Alzheimer's disease model mice. Source data are provided as a Source Data file.

examined the 18 synaptic proteins we stained, at locations that did not exhibit amyloid, which might represent proteins at putative synapses that do not contain amyloid (which might be in a different physiological or health state than synapses that did contain amyloid). We masked out Aβ, and then quantified synaptic proteins that were non-overlapping with such amyloid hotspots after additional median and size filtering (see "Methods" section). 10 out of the 18 proteins we thus analyzed were significantly decreased in 5xFAD brains (Fig. 3e, with statistical significance determined using a linear mixed effects model, $n = 8$-9 fields of view per group from 2 animals per group, see Supplementary Table 7 for full statistics). One out of the 18 proteins, GluA2, was significantly increased in 5xFAD mice compared to wild-type, where GluA2 expression visually appeared quite sparse at this age timepoint, at least relative to the higher levels seen in 5xFAD mice (Fig. 3b(ii)).

We next examined synaptic proteins that co-localized with Aβ nanoclusters, structures that cannot be observed with diffraction-limited confocal microscopy of non-expanded samples, or even with pre-expansion staining of samples that are then expanded[4]. Thus, visualization of such nanoclusters requires the epitope decrowding effect afforded by ExR and multiExR. We manually identified Aβ nanocluster ROIs in which all three Aβ stains were positive, and counted the total volume of puncta for each synaptic and Aβ channel contained in each ROI. We observed a relatively high volume occupied by GluA2 and CaMKIIa in these nanocluster ROIs (Fig. 4a, b). In contrast, the volume occupied by other synaptic proteins and PLP1 (which we added to this analysis, after visually observing it to colocalize with amyloid nanoclusters) contained within these Aβ nanocluster ROIs was smaller (see Supplementary Table 8 for descriptive statistics). Given the prominence of GluA2, we wondered if other α-amino-3-hydroxy-5-methyl-4-isoxazolepropionic acid receptor (AMPAR) subunits, i.e. GluA1, GluA3, and GluA4, were also present; GluA1 was found at trace amounts in these puncta, in terms of volume occupied, on average, GluA3 was present in a fraction of puncta, but GluA4 was present more consistently (Fig. 4b).

Given that AMPA subunits assemble in heteromeric fashion to form functional receptors, we wondered if there was any relationship between the amount of GluA2 within a Aβ nanocluster, and the amount of GluA4 found therein. Because all Aβ species imaged exhibited qualitatively similar staining patterns (Fig. 3), we arbitrarily chose to use D54D2, for this analysis, to quantify synaptic protein colocalization with amyloid. By calculating the volume of D54D2 that contained each AMPAR subunit as the intersection of GluA1/2/3/4 volume and D54D2 volume divided by total D54D2 volume, we found a significantly larger fraction of D54D2 containing GluA2 than GluA4 (Fig. 4c, $n = 44$ nanocluster ROIs from 8 fields of view from 2 5xFAD mice, Supplementary Table 9(i–ii) for statistics). We found essentially no GluA1 and very little GluA3 within D54D2 puncta (Fig. 4c). Additionally, there were many more ROIs for which there was no GluA4 contained within a D54D2 punctum, than for GluA2 (Fig. 4c, 4.55% zero for GluA2 vs. 52.3% for GluA4; Chi-squared test, Chi-square = 24.64, $p < 0.0001$, $n = 44$ nanocluster ROIs from 8 fields of view from 2 5xFAD mice). Leveraging the multiplexed nature of the data, we performed pairwise linear regressions on the volume of GluA4 and GluA2 vs. D54D2 present in Aβ nanocluster ROIs, and found that both were highly correlated, but the best-fit line for GluA2 vs. D54D2 volume was shifted up from that of GluA4 vs. D54D2 (Fig. 4d and Supplementary Table 9(ii) for full statistics). For Aβ nanocluster ROIs in which GluA4 was present, the volume of GluA2 present was correlated with that of GluA4 (Fig. 4e and Supplementary Table 9(iii) for full statistics). Visual inspection of GluA2 and GluA4 in Aβ ROIs chosen from different parts of the distributions of Fig. 4c illustrate these observations (Fig. 4f).

These results suggest non-random colocalization of GluA2, and to a lesser extent, GluA4, with Aβ nanodomains in the 12-month 5xFAD mouse brain. This colocalization illustrates the power of multiExR: given that most other synaptic proteins, and especially the other AMPAR subunits examined, GluA1 and GluA3, did not exhibit such striking colocalization with Aβ nanodomains, analyzing such pairwise and multi-way protein nanoscale coordination benefits greatly from being able to visualize many proteins in the same sample, with nanoscale precision. To our knowledge, this is the first observation of AMPAR aggregation in Aβ nanodomains in the 5xFAD mouse model, and may reflect pathological aggregation of these synaptic proteins in the context of amyloid pathology. AMPARs aggregate for synapse formation, and specific subunits affect AMPAR permeability and function. Co-aggregation of subunits with amyloid may have synaptic implications, either from altered AMPAR function or gross dysfunction.

Nanoscale multiprotein visualization of synapses

We visualized, in wild-type mice, 20 synaptic proteins important for neural architecture and transmission: the presynaptic proteins bassoon, RIM1, RIM-BP, Vglut1; the P/Q-type Calcium channel $Ca_v2.1$ alpha 1A subunit (Cav2.1); the postsynaptic scaffold proteins Shank3, SynGAP, PSD95, IRSp53, Elfn1; neurotransmitter receptor subunits GluA1, GluA2, GluA3, GluA4, NR1, and NR2B; the AMPA receptor auxiliary subunit Stargazin; the calcium/calmodulin-dependent protein kinase II alpha subunit (CaMKIIa); gephyrin, a GABA (gamma-aminobutyric acid)-ergic synapse scaffolding protein; and the tyrosine kinase receptor protein Erbb4 (Fig. 5 and Supplementary Table 10). As we previously showed[4], some of these proteins cannot be visualized well with pre-expansion staining, due to the crowded nature of synapses, but can be easily visualized with ExR because decrowding proteins facilitates their staining with conventional antibodies.

Associated registration errors, with median of 45 nm across all rounds and fields of view in 2 mice, are provided in Supplementary Table 11. This error is consistent with, and indeed a bit smaller than, that of our secondary validation dataset, which used the same reference channel and registration strategy (path 9, reference channel option **1(i)** in Supplementary Fig. 1). One round pair that failed registration using the global feature-based registration algorithm (**2(i)** in Supplementary Fig. 1c) was registered using the global intensity-based algorithm (**2(ii)** in Supplementary Fig. 1c). Images were obtained from 8 fields of view from 2 mice (Supplementary Tables 10 and 11).

Many proteins overlapped or appeared adjacent to each other, as would be expected at synapses; the composition and expression level would vary from synapse to synapse. For example, postsynaptic scaffold proteins (SynGAP, PSD95, Shank3, Homer1) colocalized with each other (see line-headed white arrows in Fig. 5) and formed sandwich-like structures between pre- (Bassoon, RIM1) and post-synaptic scaffold

https://doi.org/10.1038/s41467-024-53729-w

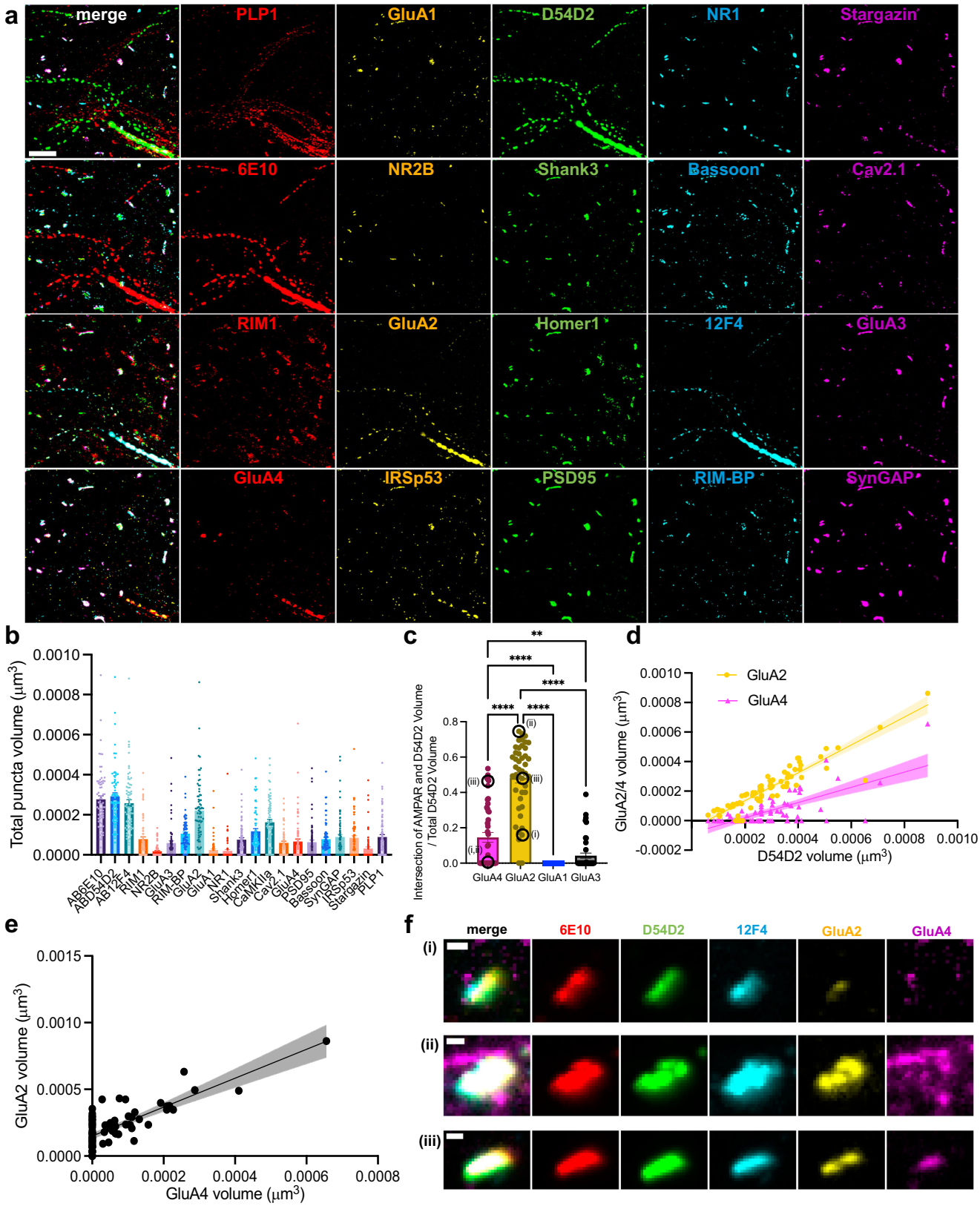

proteins (PSD95, SynGAP) (see triangle-headed white arrows in Fig. 5, zoomed into in **iii-iv**). AMPA receptor subunits (GluA1/3/4) and a transmembrane AMPA receptor regulatory protein (Tarp gamma-2, Stargazin) co-localized with each other (see blue arrows in Fig. 5). Gephyrin, a known inhibitory synaptic marker, was observed in some putative synapses with excitatory synaptic proteins nearby (AMPA receptor, N-methyl-D-aspartate (NMDA) receptor, Shank3, Stargazin, SynGAP) (see red arrows in Fig. 5). VGlut1 was more scattered than the synaptic scaffold proteins we imaged in the same volume. We observed that VGlut1 signal was relatively more diffuse compared to these other proteins after maximum intensity projection of the 3-dimensional image volume. However, examining a single z-plane

Fig. 4 | Analysis of nanoscale colocalization of synaptic proteins and amyloid-beta in Alzheimer's model mouse brain. a Example 5-channel and composite maximum intensity projections of a 5xFAD field of view, cropped to show Aβ nanoclusters. (Scale bar, 1 µm). **b** Bar plots of total volume of select proteins within Aβ nanocluster ROIs ($n = 71$ ROIs from 9 fields of view from 2 5xFAD animals; Supplementary Table 8 for full statistics, error bars indicate mean ± standard error of the mean). **c** Bar plots of the fraction of volume of D54D2 occupied by AMPA receptor (error bars are mean ± standard error of the mean, statistical significance determined by Tukey's multiple comparisons test following one-way ANOVA, $p < 0.0001$ for all asterisked comparisons except $p = 0.0047$ for GluA3 vs. GluA4, $n = 44$ nanocluster ROIs from 8 fields of view from 2 5xFAD animals; Supplementary Table 9(i) for full statistics). **d** Scatterplot of GluA2 (yellow circles) and GluA4 (blue triangles) volume vs. D54D2 volume within Aβ nanocluster ROIs. Lines indicate the best-fit lines from simple linear regressions, and the shaded regions indicate the 95% confidence interval on the best-fit line ($n = 71$ ROIs from 9 fields of view from 2 5xFAD animals; Supplementary Table 9(ii) for full statistics). **e** Scatter plot of GluA2 volume vs. GluA4 volume within Aβ nanocluster ROIs. Black line indicates the best-fit line from a simple linear regression, and the shaded region indicates the 95% confidence interval on the best-fit line (the same $n = 71$ ROIs from 9 fields of view from 2 5xFAD animals; Supplementary Table 9(iii) for full statistics). **f** Maximum intensity projections for selected channels of the ROIs circled in black in the plot in **c**. Scale bar, 50 nm. ****$p < 0.0001$, ***$p < 0.001$ **$p < 0.01$, ns, not significant. WT, wild type. 5xFAD, 5x familial Alzheimer's disease model mice. The 5xFAD data are from the same animals and fields of view as Fig. 3. Source data are provided as a Source Data file.

revealed vGlut1 colocalization with Bassoon and SynGAP, as expected (Supplementary Fig. 5). In the future, detailed analysis of multiExR synaptic data could be useful for investigators seeking to characterize synapse types and states from a heterogenous synapse population.

We also demonstrate the use of multiExR to profile putative synapses in cultured neurons, as in vitro models are widely used in neuroscience. We imaged 10 synaptic proteins over 5 staining rounds (Supplementary Table 12): Synapsin1, NR1, NR2B, SynGAP, GluA1, PSD95, Bassoon, Gephyrin, RIM1, and CaMKIIa. We observed diffuse (non-punctate), large-volume Synapsin1 immunoreactivity, colocalization of postsynaptic proteins NR2B, SynGAP, NR1, and PSD95, and very sparse and dim gephyrin immunoreactivity (Supplementary Fig. 4a, b). For registration across rounds, we stained for SMI, GFAP, and Homer in a single reference channel (path 1, reference channel option **1(ii)** in Supplementary Fig. 1), used the global feature-based registration algorithm, and achieved a median registration error of 49 nm across all fields of view and round pairs (Supplementary Fig. 4c and Supplementary Table 13). This result demonstrates that multiExR can be used to quantitatively profile nanoscale structures in cultured neurons.

Discussion

We here show that we can map many proteins in the same field of view, in the same intact specimen, with nanoscale precision, with multiExR. MultiExR builds from the high spatial resolution of ExR (~20 nm within a round (i.e., regular ExR, as previously published) with a median cross-round registration error of 39 nm across all round pairs in all datasets) with the ability to map ~20 proteins in the same field of view, in the same intact tissue (or cell culture) sample, through a multiscale staining strategy, finely tuned sample staining and washing steps, and optimized image registration pipelines. We showed the power of multiExR to reveal colocalization of glutamate receptor subunits with amyloid nanodomains in Alzheimer's model mice, and to visualize synaptic proteins in mouse cortex. MultiExR, despite its power in resolving large numbers of proteins with nanoscale precision, only requires ordinary chemical reagents, conventional antibodies, and classical microscopes (flowcharts for overall ExR workflow, and detailed choice guidance, are provided in Fig. 1 and Supplementary Fig. 1 respectively). A caveat of our technique and any technique that relies on antibody staining is that results depend on the specificity and sensitivity of the antibodies used. We relied on commercial vendors and publications to provide evidence of validation (see Supplementary Table 18 for more details). If antibody specificity is of particular concern to end users, such users can perform additional validation using knockout cell lines or tissues, or other validations appropriate to the scientific question at hand. Finally, it is important to note that multiExR image quality depends on antibody performance. To assist future users, we have provided a list of antibodies that yielded negligible signal with multiExR in the region imaged (Supplementary Table 14).

A key decision in the multiExR workflow is the choice of reference channel. We chose Lectin, a marker of blood vessels, as the millimeter-to-micron-scale reference channel, because blood vessels are present throughout the brain parenchyma, and exhibit unique morphologies that allow a researcher to visually locate the same field of view for imaging across rounds. However, we found blood vessels alone did not provide sufficient nanoscale feature density for fine-scale registration. Thus, we added neurofilament and/or glial-process markers, SMI and GFAP respectively, as well as a synaptic scaffolding protein (Homer) to the same reference channel, to facilitate nanoscale feature identification and mapping across rounds. Each of these markers is expected to be abundant in the brain areas we imaged. However, users are not limited to our choice of reference channel. Indeed, if multiExR is applied outside of the brain, in other tissues, users will have to use a different reference channel, which will need to be validated and optimized. We think any abundant, bright (high signal-to-noise), and heterogeneous (i.e., unique features at multiple length scales, from nano to macro) stain could work as a reference channel – including, potentially, a non-specific protein stain.

Many multiplexing technologies for protein visualization exist, such as cyclic immunofluorescence[16–22], fluorophore quenching[23], or use of DNA-antibody conjugates[24]. Some of these multiplexing technologies, including immunostaining with signal amplification by exchange reaction (ImmunoSABER)[25], multi-round immunostaining expansion microscopy (MiriEx)[19], magnified analysis of the proteome (MAP)[20], and decrowding expansion pathology (dExPath)[12] have been demonstrated to work with 4-fold expansion of biological specimens. Conversely, existing super-resolution imaging techniques, including stimulated emission depletion (STED)[26], structured illumination microscopy (SIM)[27], stochastic optical reconstruction microscopy (STORM)[28], and photoactivated localization microscopy (PALM)[29] are limited to five channels and therefore five proteins in a sample, owing to spectral overlap of fluorophores. Another super-resolution method, Exchange-PAINT[24,30], a variation of DNA points accumulation for imaging in nanoscale topography (DNA-PAINT)[31], can in theory be multiplexed to image more than four proteins in a single sample, but has not yet been demonstrated with 3D imaging in tissues. 3D DNA-PAINT imaging of organelles in cell cultures has been achieved[32,33]. However, these studies were only shown with 2–3 channel multiplexing in cell cultures.

Narayanasamy et al. demonstrated Exchange-PAINT for super-resolution imaging of synapses in tissue[34]. However, this approach was only shown with 2-dimensional images and is limited by the number of available secondary antibodies with compatible species. Another approach, multiplexed automated serial staining stochastic optical reconstruction (maS^{3}STORM), demonstrated 3D super-resolution imaging of 16 targets in central nervous system (CNS) tissue, but requires a direct stochastic optical reconstruction microscopy (dSTORM)-capable microscope[35]. Yet another method, molecule anchorable gel-enabled nanoscale imaging of fluorescence and stimulated Raman scattering microscopy (MAGNIFIERS) achieved 8-plex 3D nanoscale imaging in a mouse brain slice, but requires a Raman microscope[36]. All of these approaches require custom DNA-conjugated

https://doi.org/10.1038/s41467-024-53729-w

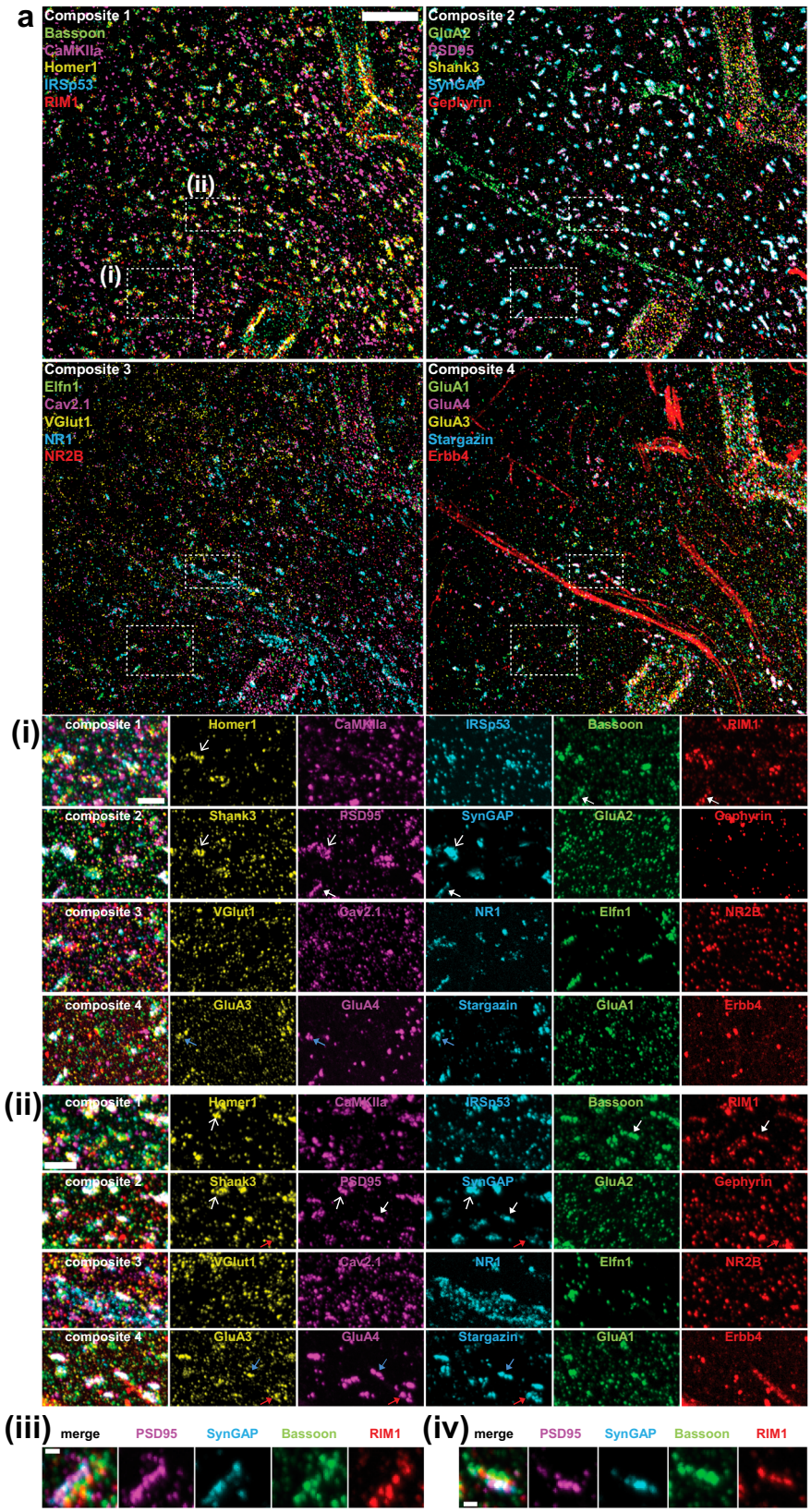

antibodies, custom imaging reagents, and/or advanced hardware such as total internal reflection fluorescence (TIRF) illumination systems, which are not readily available in most biology and neuroscience laboratories.

By comparison, multiExR can generate 3-dimensional, 20+ channel, super-resolution images of proteins in tissue sections, using widely available reagents and an inverted confocal microscope. MultiExR enables nanoscale imaging, with potentially very high multiplexing capacity, requiring only ordinary microscopes and common laboratory reagents. But the high resolution of ExR demands staining, washing, and registration strategies up to the challenge of nanoscale alignment, realized in this current paper. We note there is a speed

Fig. 5 | 20-plex nanoscale characterization of synapses in the mouse somatosensory cortex. a Example composite 5-channel maximum intensity projection a field of view showing synaptic proteins in mouse somatosensory cortex obtained using multiExR (from one of two mice from one batch of experiments). Scale bar, 2 μm in biological units. **i–ii** Single-channel and composite maximum intensity projections of synaptic proteins in the boxed regions from (**a**). Line-headed arrows indicate colocalized postsynaptic scaffold proteins; triangle-headed arrows indicate sandwich-like structures between pre- and postsynaptic scaffold proteins; red arrows indicate gephyrin with excitatory synaptic proteins nearby; blue arrows indicate colocalized AMPA receptors with transmembrane AMPA receptor regulatory proteins (Tarp gamma-2, Stargazin)). Scale bar, 500 nm in biological units. iii-iv Single-channel and composite maximum intensity projections of synaptic proteins forming sandwich-like structures from (i)-(ii). Scale bar, 100 nm in biological units.

versus measurement error tradeoff with multiExR (Supplementary Fig. 1). There is a relationship between choice of reference channel and protocol duration: dedicating more optical channels to reference stains improves registration quality at the cost of the number of target stains that can be imaged per round. It may take several weeks to acquire a 20-protein dataset with an average registration error of ~40 nm. Thus, the method may not be practical for certain applications, such as for large-sample size confirmatory experiments, especially when 4 or fewer protein targets need to be imaged. For such experiments, classical ExM or ExR may be more appropriate. As mentioned in the discussion and demonstrated in Figs. 3–5, multiExR may be most useful as a hypothesis-generating, exploratory technique, analogous to other high-resolution spatial multiplexing techniques (e.g. expansion sequencing[8]), which also require weeks for data acquisition. As with other cyclic immunofluorescence-based methods, speed bottlenecks include overnight incubations for primary and secondary antibodies and time spent imaging. If speed is a priority, users could consider shortening antibody incubation time (e.g., 2 hours at room temperature for secondary antibodies; though a shorter incubation time would need to be tested empirically for each primary and secondary antibody) or imaging a small, targeted, set of regions of interest to shorten imaging time.

The appropriateness of multiExR for an experiment depends on the required measurement scale for the underlying biological question and the distribution of registration errors achieved for a given image. That is, what is the minimum distance between puncta (for example) that one needs to measure, below which two things are considered indistinguishable, and above which things are considered separate? One useful observation is: registration error is not constant throughout an image, and thus regions can be found that enable higher precision measurements than others. For example, if 95% of the calculated registration error values fall within the range of 34-37 nm (as for one round pair in Supplementary Table 6), then a user can with 95% confidence measure distances 54-57 nm in size (taking measurement error to be registration error + resolution). We provide information on the distribution of registration errors we achieved for each field of view in each round pair in Fig. 2f, Fig. 3c, Supplementary Fig. 3b, Supplementary Fig. 4c, and Supplementary Tables 2, 4, 6, 11, and 14. The software we provide calculates 1000 estimates of registration error for every field of view (one for each randomly sampled subvolume above a signal threshold, see Methods), enabling the user to estimate the distribution of registration errors in the image. Should a reader want to examine only portions of the image that fall within a given registration error range (for example, 30 nm or less), they can crop the image to regions with registration error in this range (Supplementary Fig. 7). Given the right-skew of the distributions of registration error that we found (Fig. 2f, Fig. 3c, Supplementary Fig. 3b, Supplementary Fig. 4c), the majority of the field of view could be in an acceptable range depending on the biological question at hand.

In principle, a total protein stain such as N-hydroxysuccinimidyl(NHS)-ester bearing a fluorophore could make an excellent reference stain, as it labels densely and across scale, as is being explored for expansion-based connectomics[37]. In practice, we found that NHS-ester staining (e.g., an overnight incubation with 2 μM NHS-ester dye (Atto 647 N NHS ester, Millipore Sigma 18373) in NHS ester staining buffer (5x SSCT, 5x SSC + 0.1% Tween 20) on a shaker at RT, and washing three times in 5x SSCT for 30 min each at RT)[38]) was different enough from our antibody staining condition, that we were concerned that it would add additional complexity to the protocol beyond what it exhibits now. Given that our antibody-based reference channel strategy could achieve small registration errors, we did not pursue NHS-ester staining further, in the current study.

Alzheimer's Disease is a devastating neurodegenerative disorder marked histopathologically by synapse loss, amyloid-beta plaques, and tau neurofibrillary tangles[39,40]. 5xFAD mice were engineered to carry 5 familial Alzheimer's Disease mutations in amyloid precursor protein and presenilin, which increase the production of Aβ plaque formation, to model Alzheimer's Disease pathology in an accelerated manner[13]. We used multiExR to examine Aβ and synapse pathology in 5xFAD mouse cortex, comparing the expression and localization of 23 different proteins relative to wild-type mouse cortex. This approach, which detects the nanoscale localization of 12F4, 6E10, and D54D2 species, which identify different isoforms and conformations of Aβ, provides a simple-to-execute alternative to previous approaches to detect Aβ in synapses, such as array tomography and STORM[41]. As has been found previously[42,43], we observed dramatic synapse alteration in 5xFAD mouse cortex, marked by reduction in number and volume of several proteins. Finally, we observed colocalization of synaptic proteins and Aβ nanoclusters, in particular GluA2 and GluA4. This finding is in line with previous work showing deficits in AMPA receptor function after amyloid exposure[41,44,45] and may reflect pathological aggregation of synaptic proteins in the 5xFAD brain, similar to what we observed with Nav and Kv channels in our previous work[4]. Our comparison of 5xFAD and WT brains demonstrate the utility of multiExR in detecting and quantifying previously unappreciated nanoscale, multi-protein pathology in disease states.

The synapse is a densely packed biomolecular environment where thousands of proteins interact to facilitate rapid synaptic transmission and downstream signaling cascades. Synaptic proteins are numerous, often form complexes with one another, and are often mutated in psychiatric and neurodevelopmental disorders[46,47]. Understanding the abundance and (co)localization of these proteins at the synapse is critical to our understanding of neuronal communication in healthy and disease states. To demonstrate the utility of multiExR in visualizing synaptic proteins towards this purpose, in a second demonstration, we visualized 20 synaptic proteins in the same tissue specimen of the mouse somatosensory cortex. In the future, detailed analysis of such high-dimensional datasets could facilitate the classification of synapse types and states. Nanoscale multi-protein colocalization as revealed by multiExR could be used to generate novel hypotheses regarding protein-protein interactions.

Methods

Brain tissue preparation

All procedures involving animals were in accordance with the US National Institutes of Health Guide for the Care and Use of Laboratory Animals and approved by the Massachusetts Institute of Technology Committee on Animal Care. Mice housing condition is normal dark/light cycle, ambient temperature, and humidity. Both male and female wild-type (WT) ($n = 3$ C57BL/6, 6-8 weeks of age, from JAX), aged WT ($n = 2$ C57BL/6, 12-13 months of age), and 5xFAD mice ($n = 2$, 12-13 months of age, from the Mutant Mouse Resource and Research

Center) were deeply anesthetized using isoflurane in room air. Mice were perfused transcardially with ice-cold 15 mL of 2% (w/w) acrylamide (AA) in phosphate-buffered saline (PBS) followed by 15 mL of 23.2% (w/w) acrylamide (AA) and 2.7% (w/w) paraformaldehyde (PFA) in PBS (e.g., 15 g acrylamide added in 32.5 mL deionized water with 5 mL 10x PBS and 12.5 mL 16% PFA solution). Brains were harvested and post-fixed in the same fixative overnight at 4 °C. Fixed brains were transferred to 100 mM glycine for 6 hrs at 4 C, then transferred to PBS. The brain regions for expansion were dissected from 50-100 μm free-floating slices cut on a vibrating microtome (Leica VT1000S) in PBS. Sagittal sections were used for Figs. 3 and 4, and coronal sections were used for all others. Considering that the final expansion will be 18-20-fold, it is recommended that the starting tissue size is smaller than 3 × 3 mm for easy handling.

Cultured neuron preparation

Cultured mouse hippocampal neurons were prepared from postnatal day 0 or 1 Swiss Webster mice (Taconic, both male and female mice) as previously described[48]. The coverglasses in the 24-well plates were pre-treated with diluted Matrigel (250 μL Matrigel in 12 mL DMEM (Dulbecco's Modified Eagle Medium)), and 160,000-200,000 cells were plated in each well. Neurons were grown for 14 d to 1 month in the incubator (37 °C and 5% CO2 in a humidified atmosphere). For fixation, neurons were briefly washed with PBS, and fixed with 4% PFA in PBS for 10 min at room temperature and 0.61% (w/w) PFA + 1% acrylamide in PBS for 6 h at 37 °C. After washing with PBS, samples were stored at 4 °C before expansion.

Expansion of brain tissue slices and cultured neurons

The first gelling solution was prepared (7.4% (w/w) sodium acrylate (SA), 2.5% (w/w) AA, 0.08% (w/w) *N*,*N*′-methylenebisacrylamide (Bis), 0.2% (w/w) ammonium persulfate (APS) initiator, 0.16% (w/w) tetramethylethylenediamine (TEMED) accelerator, and 0.01% (w/w) 4-Hydroxy-TEMPO (4HT)) and 2M NaCl in 1x PBS base without adding APS. The dissected brain slice or cultured neuron plated coverglass was placed between two #1.5 coverslips separated by two pieces of #1.5 coverslips. After vortexing the gelling solution with APS, the excess gelling solution was added around the tissue. After incubation at 4 °C for 30 min, the sample was incubated at 37 °C for 30 min to 2 hrs until gel formation. The tissue or neuron-containing gel was obtained by trimming excess gel. It is helpful to cut the gel into an asymmetric shape to maintain tissue orientation. The gel was incubated in denaturation buffer (200 mM sodium dodecyl sulfate (SDS), 200 mM NaCl, and 50 mM Tris pH 8) for 1 h at 95 °C using a thermocycler. The denatured gel was placed in 6-well plates and washed at least twice using deionized water (DIW) for 15 min each. For the re-embedding step, expanded 1st gel was placed in 6 well plate and incubated in the re-embedding solution (13.75% (w/w) AA, 0.037% (w/w) Bis, 0.023% (w/w) APS, 0.02% (w/w) TEMED) twice for 1 h each on the shaker at room temperature. The first re-embedding solution was replaced with a freshly made second re-embedding solution. The gel was transferred and placed between coverslips, avoiding bubble formation. The gel chambers were placed in a plastic zipper storage bag for 5 min nitrogen purging and incubated for 1–2 hrs at 45 °C. For the 3rd gelling step, the re-embedded gel was placed in a 6 well plate and incubated in the 3rd gelling solution (7.4% (w/w) SA, 2.5% (w/w) AA, 0.04% (w/w) Bis, 0.023% (w/w) APS, and 0.02% (w/w) TEMED and 2M NaCl in 1x PBS) twice for 1 h each on the shaker at room temperature. The gel was transferred and placed between coverslips with the additional gelling solution to avoid bubbles. The gel chambers were placed in a plastic zipper storage bag for 5 min nitrogen purging and incubated for 1 h at 60 °C. The gel was transferred to a petri-dish with DIW. The gel was fully expanded in DIW by overnight incubation and changing excess water 2–3 times per 2 hrs on the following day. The gel was trimmed axially from the tissue or neuron-containing portion at the bottom to reduce the thickness to 1 mm to facilitate subsequent immunostaining and imaging. We opted to further stabilize the trimmed gel for using additional re-embedding step with reduced AA concentration (2% (w/w) AA, 0.037% (w/w) Bis, 0.023% (w/w) APS, 0.02% (w/w) TEMED) so as to maintain gel integrity during multiple rounds staining, stripping, and imaging.

Immunostaining of expanded tissues

The gel was incubated in blocking buffer (0.5% Triton X-100, 5% normal donkey serum (NDS) in PBS) for 1–2 hrs at room temperature. The gel was incubated with primary antibodies in staining buffer (0.25% Triton X-100, 5% NDS in PBS) overnight at 4 °C. The gel was washed in 1x PBST washing buffer (0.1% Triton X-100 in 1x PBS) 6 times for 30 min each on a shaker at room temperature. The gel was incubated with secondary antibodies in staining buffer overnight at 4 °C, and washed in 0.05x PBST washing buffer (0.1% Triton X-100 in 0.05x PBS) 6 times for 30 min each on a shaker at room temperature. The antibodies against three target proteins per round were stained with 488, 546, and 633 nm channels, and the Lycopersicon Esculentum Lectin with 594 nm channel (Vector Laboratories, DL-1171-1) was co-stained every round to serve as a reference channel. The images of the multi-ExR sample were obtained using a Nikon CSU-W1 or SORA confocal microscope with 100% laser power and 1 s exposure time per channel. The global tiled image using 4x and 10x objectives and Element software with annotation of ROI marking were used to find the same field of view over multiple rounds imaging. The same field of view is located and re-imaged through the following process. In the first round of staining and imaging, we obtain a large (~500um x 500um, covering most of the gel) mosaic image of the reference channel, followed by an image of a smaller region of interest, both with the 10x objective. These mosaic images of the reference channel are used to guide the experimentalist in finding the same field at increasing magnification in later rounds using the same reference channel. The 40x water immersion objective was used to collect the fields of view shown in the manuscript with a 0.25 μm z-step size. The gel was placed on the glass bottom 6 well plate, covered with plate-sealing film for 30 min before starting the imaging session to stabilize the gel to prevent drifting during image collection. For the stripping of antibodies, the gel was incubated in denaturation buffer with 100 mM beta-mercaptoethanol for 1 h at 95 °C and washed 4 times with excess PBS. The next round of immunostaining was repeated by blocking, staining, imaging, and stripping the gel as described.

Expansion factor measurement

The 20x expansion factor for ExR has been demonstrated previously[4]. A second re-embedding step was added after the final expansion to strengthen the gel for multi-round gel handling. To determine the effect of second re-embedding on the expansion factor, we measured gel size after the second re-embedding. Before the second re-embedding step, six gels were excised to the height of 1.5 cm. For the second re-embedding step, expanded 3rd gels were incubated in re-embedding solution (2% (w/w) AA, 0.037% (w/w) Bis, 0.023% (w/w) APS, 0.02% (w/w) TEMED) twice, replacing the first solution with freshly made re-embedding solution for 1 h each time on a shaker at room temperature. The second re-embedded gels were washed in 0.05x PBST washing buffer (0.1% Triton X-100 in 0.05x PBS) 4 times for 1 h each on a shaker at room temperature, then the size of gels were measured, and decreased by 10% on average, leading to a final expansion factor of 18x.

Image preprocessing and registration

All custom image processing and analysis scripts for all analyses in this manuscript are available at https://github.com/schroeme/multi-ExR. First, background was subtracted from image stacks using ImageJ/Fiji's Rolling Ball algorithm with a radius of 50 pixels. After background

subtraction, images from later rounds were registered in x, y, and z space to the first imaging round (Fig. 1c). One or more channel(s), always including the reference channel (whether single or three-stain), were designated to serve as the reference channel between subsequent rounds. We created a toolbox for both global and local alignment of multiExR imaging rounds, consisting of (with reference to Supplementary Fig. 1: **1(i)** a 3D scale-intensity feature transform (SIFT)-based global registration algorithm previously used for multiround RNA multiplexed-imaging alignment (ExSeqProcessing registration[8,9]), **1(ii)** an alternative intensity-based global registration algorithm (Elastix[10]), and **1(iii)** a point-based alignment step for refinement of local structures such as synapses (Fig. 1c).

(1) Feature-based global registration. The first is a previously-described algorithm utilizing 3D scale-invariant feature transform (SIFT) for keypoint detection and a 3D affine transform[8,9], available at https://github.com/dgoodwin208/ExSeqProcessing. Briefly, keypoints are detected, features are constructed, subsequently matched between image volumes. These matched features are used to calculate a warp for one image into the space of another. For all datasets, the first imaging round was used as the reference round for registration. We used the following parameters from the publicly available ExSeqProcessing repository registration pipeline: downsample_rate = 4 and pyramid_scale = [1:9]. For the staining rounds of all fields of view from the validation dataset (Fig. 2), the four fluorescence channels were normalized and summed to serve as the reference channel, per the default ExSeqProcessing configuration. For the stripping rounds of the primary validation dataset, all rounds of the secondary validation dataset, and all rounds from the synaptic dataset, only the multi-protein reference channel was used to detect features and calculate the warp. For the 5xFAD dataset, all channels were used as reference channels, but they were not normalized and summed prior to feature detection, as this was found empirically to improve registration quality. For difficult registrations, we recommend trying a variety of registration configurations, including using one or multiple channels as reference, with and without normalization, as described in Supplementary Fig. 1. The ExSeqProcessing pipeline was run using cuda = True on a GeForce RTX 2080 Ti GPU, allowing multiple fields of view to be registered in a few hours.

(2) Intensity-based global registration. Expansion microscopy images of the brain often contain neural structures with various scales, which is challenging to align well simultaneously. Thus, for empirically difficult (i.e., noisy or highly shifted between rounds) fields of view that could not be registered using the ExSeqProcessing pipeline, we implemented an alternative intensity-based method for coarse structures, available at https://github.com/donglaiw/ExM-Toolbox/tree/ck/mExR. We first pre-processed the image volumes to remove fine structures and image noise with the Non-Local Means denoising method (Supplementary Note 1) and then the adaptive thresholding method (Supplementary Note 2) to mask them out. Then, we used the Elastix[10] package to estimate the global affine transformation by minimizing the mutual information of the intensity of matched voxels. Finally, we use the first-order B-Spline Interpolator with the estimated transformation to compute the spatial mapping. We used this registration method for four rounds in one field of view in the secondary validation dataset (Supplementary Fig. 3), for one round in one field of view in the synaptic dataset (Fig. 5), for several fields of view obtained in earlier optimization experiments that were not included in this manuscript, and for some other fields of view in this to confirm its utility (Supplementary Fig. 6).

(3) Point-based local registration. After the global alignment of coarse structures, we aimed to improve the registration of fine-scale structures of interest, e.g., synapses. We first extracted synapses by removing image noise with Non-Local Means denoising, followed by the adaptive thresholding method to mask both the noise and the coarse structures. Then, we computed the centroid of synapses to obtain a point cloud for each volume. Next, we applied the Iterative Closest Point (ICP) algorithm (Supplementary Note 3) to find point matches and compute affine transformation iteratively. Finally, we used the radial basis function (RBF) for interpolation to generate a dense deformation field from the sparse matches[11] (Supplementary Note 4). The dense deformation field thus produced is used for interpolating pixels in the coordinate space, which yields the warped volume. A tutorial for this method is provided at: https://github.com/donglaiw/ExM-Toolbox/blob/ck/mExR/tutorial.ipynb.

For experiments in this manuscript, we mostly used the feature-based global alignment method (**3(i)** in Supplementary Fig. 1c, ExSeqProcessing registration), which produced registered images in an acceptable error range for the demonstration of our technology. However, during development, we noticed that the intensity-based global alignment (**2(ii)** in Supplementary Fig. 1c) sometimes works well on failure cases in the feature-based method (Supplementary Fig. 6a-c). In addition, the point-based local alignment step (**2(iii)** in Supplementary Fig. 1c) can improve synapse alignment (Supplementary Fig. 6d). Thus, we provide all methods here as a toolbox, from which users can choose the best-performing set of algorithms for their data.

Quantification of registration accuracy

To avoid image stack edges that were empty for some imaging rounds after registration (because warping often involved translation in the z-axis), image volumes were cropped to a 61-slice stack of mutually overlapping volume for each round. Registration accuracy was quantified based on a previously described method[8]. For the primary validation dataset, we chose to quantify registration error using the SynGAP channel, which had higher SNR than the bassoon channel (Fig. 2). For the secondary validation dataset, we quantified registration error using the 4-stain reference channel, to be consistent with later experiments where only the reference channel is available to calculate registration error. For the synaptic and 5xFAD datasets, we used the multi-channel reference channel to quantify registration error. Volumes were converted to grayscale and cropped to slices with at least one nonzero pixel. Then, we calculated a normalized cross-correlation of 1,000 subvolumes (each of size $100 \times 100 \times 61$ pixels), randomly chosen across the imaged field of view, excluding the edges ($18.5 \times 18.5 \times 0.85$ microns in size, in biological units). All subvolumes analyzed had greater than 1% of voxels above an intensity threshold of the 99th percentile intensity of the whole field of view. The registration error was calculated as the mean of the offsets in maximum normalized cross-correlation between each pair of rounds for each subvolume in each dimension. Violin plots of estimated population density were created in GraphPad Prism, and outliers were removed using the ROUT method (Q = 1%).

Calculation of feature density in the reference channel

This analysis was performed on unregistered images. A binary mask of each channel was created as follows: conversion to grayscale (min-max normalization using MATLAB's "mat2gray"), binarization using a threshold at the 99.5th percentile value of the volume intensity distribution, and removal of connected components smaller than $50 \times 50 \times 50$ nm^3 in size. The reference channel mask was taken as the union (using MATLAB's "or" function) of all individual channels. We then identified 3D-connected components from the binary stack using

MATLAB's "bwconncomp" function, with a pixel connectivity of 26, meaning that pixels are connected if their faces, edges, or corners touch. Fraction of volume occupied by the reference channel was calculated as the number of nonzero pixels in the mask divided by the total number of pixels in the volume. Minimum (maximum) feature size percentage was calculated as the number of nonzero pixels in the smallest (largest) connected component (Supplementary Table 1).

Analysis of primary 7-round validation dataset

To avoid image stack edges that were empty for some imaging rounds after registration (because warping often involved translation in the z-axis), image volumes were cropped to a 61-slice stack of mutually overlapping volume for each round. To quantify the stripping and restaining efficiency of the validation dataset, in which the SynGAP and Bassoon were repeatedly stripped and stained over seven rounds using the same experimental conditions and microscope settings (Fig. 2), we automatically identified and counted putative synapses. The binary image was created as follows: conversion to grayscale, binarization using a threshold at the 99.5th percentile intensity value, median filtering with a radius of 9x9x3 pixels, subtraction of the Lectin channel mask, morphological closing using a disk structuring element of radius 250 nm, size filtration with a lower limit of 50x50x50 nm^3. The mask of the Lectin channel was created as follows: conversion to grayscale, binarization using a threshold at the 99.5th percentile intensity value, median filtering with a radius of 9x9x3 pixels, and morphological closing using a disk structuring element of radius 2 μm. We then identified 3D connected components from the filtered binary stack using MATLAB's "bwconncomp" function, with a pixel connectivity of 26, meaning that pixels are connected if their faces, edges, or corners touch. Objects (putative synapses) were defined as 3D connected components of the filtered, binary image volume (Fig. 2c).

In order to determine whether nanoscale synaptic properties were maintained over seven rounds of stripping and staining, we quantified the number of puncta, mean puncta volume, and brightness (as measured by absolute intensity and SNR) of manually-identified synaptic ROIs (Fig. 2d, e and Supplementary Fig. 2b, c). Two-dimensional ROI boundaries were selected in Fiji using the rectangle tool, based on the presence of both Bassoon and SynGAP staining in the first round. The ROI was cropped in 2 dimensions using the x- and y- boundaries from Fiji's ROI manager, with the z-boundary extending 15 slices in each direction from the center plus one frame. Synaptic ROIs were processed as follows: conversion to grayscale, binarization using a threshold at the 99.5th percentile intensity value, and size filtration to remove puncta less than 20x20x20 nm^3, which are likely noise. Synaptic protein puncta were defined as 3D connected components of the filtered, binary image volume (pixel connectivity of 26). Puncta volume was calculated from the binary mask volume using MATLAB's "regionprops3" function, multiplied by an average voxel size conversion factor of 1.2073 ×10^{-6} um^3 per voxel (weighted average of x, y, and z spatial sampling in post-expansion units, cubed). SNR was calculated as the mean intensity in the masked region (within synaptic protein puncta) divided by the mean intensity in the inverse of the masked region (within the background). Mean absolute intensity was calculated as the mean intensity of pixels within the masked region.

Quantification of 5xFAD vs. WT datasets

To avoid image stack edges that were empty for some imaging rounds after registration (because warping often involved translation in the z-axis), image volumes were cropped to a 61-slice stack of mutually overlapping volume for each round. To quantify the volume of Aβ species (Fig. 3d), image volumes for each of the Aβ channels were processed as follows: binarization using an absolute intensity threshold (Supplementary Table 15), determined based on 5 standard deviations above the mean intensity of the 5xFAD fields of view, 3D median filtering with radius 5x5x3 voxels (in x, y, and z, respectively), subtraction of the reference channel, to avoid quantification of non-specific staining along blood vessels, and exclusion of small objects (likely noise) under 100 voxels in volume. The mask of the reference channel was created as follows: binarization using a threshold at the 99th percentile intensity value, median filtering with a radius of 5x5x3 pixels, and morphological closing using a disk structuring element of radius 10 pixels. Total volume was calculated as the number of nonzero pixels in the binarized image volume, multiplied by an average voxel size conversion factor of 1.2073 ×10^{-6} um^3 per voxel (cube of weighted average of x, y, and z spatial sampling rates).

To quantify differences in synaptic protein expression between 5xFAD and WT mice (Fig. 3e), synaptic channel image volumes were processed as follows: binarization using an absolute threshold (Supplementary Table 16), determined based on 5 standard deviations above the mean intensity of the dimmest WT field of view, 3D median filtering with radius 5x5x3 voxels (in x, y, and z, respectively), subtraction of the reference channel, to avoid quantification of non-specific staining along blood vessels, size filtration to include only puncta with volume greater than 100 voxels and less than 5000 voxels. The mask of the reference channel was created as described above, but with a disk structuring element of radius 10 pixels. The number of objects and total volume in each synaptic channel were calculated as described above. For quantifying effect size, we used a linear mixed effects model (Python's statsmodels[49] "mixed_lm") to avoid type I error due to pseudoreplication. The model was set up as follows: model = smf.mixedlm("Vol ~ Group", data, groups=data["Animal"]), where "Animal" indicates animal ID, and "Group" assignment was either WT or 5xFAD. Jupyter notebooks with relevant code are available at https://github.com/schroeme/multi-ExR.

We analyzed colocalization of Aβ species and synaptic proteins in 5xFAD brains within manually-identified ROIs containing Aβ nanoclusters (Fig. 4). The ROI was cropped in 2 dimensions using the x- and y- boundaries from Fiji's ROI manager, with the z-boundary extending 18 slices in each direction from the center plus one frame. The volume and number of puncta of each protein were calculated as described above, after binarization using a threshold of 4 standard deviations of the mean intensity within the nanocluster ROI, 3D median filtering with radius 5x5x3 voxels, and size filtration with a minimum volume of 20 voxels. The fraction of volume mutually overlapped with D54D2 for GluA1-4 (Fig. 4c) was calculated as the number of nonzero pixels in the intersection between GluA1-4 and D54D2 binary masks, divided by the number of nonzero pixels in the D54D2 binary mask. For this analysis, a size filter of 20 voxels was also used. For overlap colocalization analysis (Fig.4c), we excluded ROIs with visible offset between the Aβ channels, representing residual registration error, and kept 44/71 ROIs from 8/9 fields of view.

Choice of median and size filters for nanoscale synaptic and Aβ puncta

The reader will note that the median and size filters used in the analyses described above are varied, depending on the biological goal at hand. Our selection of size filter for each of these analyses was based on empirical findings related to what produced a reasonable mask to exclude high spatial frequency noise based on visual inspection, as well as the expected size of a synapse (e.g., the synaptic cleft is about ~20 nm). Too strict a size filter (e.g., requiring puncta to be >150 voxels or 50-60 nm) leads to exclusion of puncta within actual synapses, while too permissive a size filter (e.g., <1 voxel or <10 nm) may be ineffective at removing high spatial frequency noise. We acknowledge that thresholding followed by filtration-based methods of puncta/synapse identification are, due to inevitable variability, bound to produce some false positives and false negatives. This is why we used manually-identified ROIs for detailed analyses within putative synapses or beta-amyloid nanoclusters, and decreased the size filter used on manually-

selected ROIs to reduce the chance of excluding actual puncta in such regions, which we are confident contain the biological structures of interest. To investigate the effect of our choice of size filter on our results, we conducted four parameter scans as detailed below, the results of which are summarized in Supplementary Fig. 8.

1. We calculated signal-to-noise ratio in the validation dataset (Supplementary Fig. 2b) with various size filters in the staining rounds. The size filters tested were chosen to span the range from 0 (no size filter) to 191 voxels (60 ×60 x 60nm^3; Supplementary Fig. 8a)
2. We calculated total puncta volume of synaptic proteins within manually-identified beta-amyloid nanoclusters (Fig. 4b) with various size filters, chosen to span the range from 0 to 100 voxels (Supplementary Fig. 8b). We chose to proceed with a filter of 20 voxels, because this was the largest filter for which no amyloid-beta puncta, the basis of which these ROIs were manually identified, were excluded based on size.
3. We calculated the fraction of D54D2 volume occupied by GluA2 (Fig. 4c), with various size filters applied to both channels, ranging from 0 (no filter, which is what we report in the manuscript) to 180 voxels (over double what was used for the analysis in Fig. 4b, see Supplementary Fig. 8c). We chose a size filter of 20 voxels to be consistent with the analysis in Fig. 4b.
4. We calculated the fraction of D54D2 volume occupied by GluA1-4 (Fig. 4c) both with and without a median filter of size 5x5x3 voxels, using a size filter of 20 voxels (Supplementary Fig. 8d). Eliminating the median filter did not affect the pattern of which AMPAR subunits had the most colocalization with D54D2, but did increase the numerical value of the fraction of D54D2 volume containing GluA1-4, especially in the case of GluA3. With no median filter, there were still more ROIs for which there was no GluA4 contained within a D54D2 punctum than for GluA2 (0% for GluA2 vs. 22.7% for GluA4; Chi-square = 11.28, p = 0.0008, n = 44 nanocluster ROIs from 8 fields of view from 2 5xFAD mice). Furthermore, with no median filter, conclusions based on the linear regressions shown in Fig. 4d and Fig. 4f are unchanged. We chose to proceed with a median filter to be consistent with other analyses in the paper.

The results from these tests suggest that within a certain range, the choice of size or median filter does not greatly affect our results or conclusions, but is a choice that each user should tailor as appropriate for their biological question.

Reagents
Lists of reagents used in this study, as well as the composition of gelling and denaturation solutions, are provided in Supplementary Tables 17-19.

Statistics and reproducibility
No statistical method was used to predetermine sample size for this study. In some experiments, channels with poor staining quality (very low detectable signal) or that were imaged in an earlier staining round were excluded, as detailed in Supplementary Tables 5 and 10. Rationale and methods for excluding data during analysis (e.g., ROIs with high registration offset and outliers in registration error quantification) are described above. The experiments were not randomized, nor were experimenters blinded to genotype during data acquisition or analysis.

Reporting summary
Further information on research design is available in the Nature Portfolio Reporting Summary linked to this article.

Data availability
Preprocessed, registered data are available for download from Harvard Dataverse at https://doi.org/10.7910/DVN/JJBULY. Processed data derivatives used to generate plots (i.e. Source Data, in Excel format) are available for download with this paper. Blank cells in the Source Data files are from outliers removed as described in the Methods section. Source data are provided with this paper.

Code availability
All custom image processing and analysis scripts for all analyses in this manuscript are available at https://github.com/schroeme/multi-ExR (v0.1, https://zenodo.org/records/13646611), https://github.com/dgoodwin208/ExSeqProcessing, and https://github.com/donglaiw/ExM-Toolbox/tree/ck/mExR (https://zenodo.org/records/13750923).

References

1. Good, M. C., Zalatan, J. G. & Lim, W. A. Scaffold proteins: Hubs for controlling the flow of cellular information. *Science (80-)* **332**, 680–686 (2011).
2. Chen, F., Tillberg, P. W. & Boyden, E. S. Expansion microscopy. *Science (80-)* **347**, 543–548 (2015).
3. Wassie, A. T., Zhao, Y. & Boyden, E. S. Expansion microscopy: principles and uses in biological research.*Nat. Methods* **16**, 33–41 (2018).
4. Sarkar, D. et al. Revealing nanostructures in brain tissue via protein decrowding by iterative expansion microscopy. *Nat. Biomed. Eng.* **6**, 1057–1073 (2022).
5. Hickey, J. W. et al. Spatial mapping of protein composition and tissue organization: a primer for multiplexed antibody-based imaging. *Nat. Methods* **19**, 284–295 (2021).
6. Shi, L. et al. Highly-multiplexed volumetric mapping with Raman dye imaging and tissue clearing. *Nat. Biotechnol.* **40**, 364–373 (2022).
7. P. Zrazhevskiy, X. G. Quantum dot imaging platform for single-cell molecular profiling. *Nat. Commun.* **4**, 1–12 (2013).
8. Alon, S. et al. Expansion sequencing: spatially precise in situ transcriptomics in intact biological systems. *Science (80-)* **371**, eaax2656 (2021).
9. Murray, E. et al. Simple, scalable proteomic imaging for high-dimensional profiling of intact systems. *Cell* **163**, 1500–1514 (2015).
10. Klein, S., Staring, M., Murphy, K., Viergever, M. A. & Pluim, J. P. W. Elastix: a toolbox for intensity-based medical image registration. *IEEE Trans. Med. Imaging* **29**, 196–205 (2010).
11. Rohr, K., Cathier, P. & Wörz, S. Elastic registration of electrophoresis images using intensity information and point landmarks. *Pattern Recognit.* **37**, 1035–1048 (2004).
12. Valdes, P. A. et al. Improved immunostaining of nanostructures and cells in human brain specimens through expansion-mediated protein decrowding. *Sci. Transl. Med.* **16**, eabo0049 (2024).
13. Oakley, H. et al. Intraneuronal β-amyloid aggregates, neurodegeneration, and neuron loss in transgenic mice with five familial Alzheimer's disease mutations: potential factors in amyloid plaque formation. *J. Neurosci.* **26**, 10129–10140 (2006).
14. Iaccarino, H. F. et al. Gamma frequency entrainment attenuates amyloid load and modifies microglia. *Nature* **540**, 230–235 (2016).
15. Mucke, L. & Selkoe, D. J. Neurotoxicity of amyloid β-protein: synaptic and network dysfunction. *Cold Spring Harb. Perspect. Med.* **2**, a006338 (2012).
16. Gerdes, M. J. et al. Highly multiplexed single-cell analysis of formalinfixed, paraffin-embedded cancer tissue. *Proc. Natl Acad. Sci. USA* **110**, 11982–11987 (2013).
17. Stack, E. C., Wang, C., Roman, K. A. & Hoyt, C. C. Multiplexed immunohistochemistry, imaging, and quantitation: a review, with an assessment of Tyramide signal amplification, multispectral

imaging and multiplex analysis. *Methods* https://doi.org/10.1016/j.ymeth.2014.08.016. (2014)
18. Lin, J. R., Fallahi-Sichani, M. & Sorger, P. K. Highly multiplexed imaging of single cells using a high-throughput cyclic immunofluorescence method. *Nat. Commun.* **6**, 1–7 (2015).
19. Shen, F. Y. et al. Light microscopy based approach for mapping connectivity with molecular specificity. *Nat. Commun.* **11**, 1–12 (2020).
20. Ku, T. et al. Multiplexed and scalable super-resolution imaging of three-dimensional protein localization in size-adjustable tissues. *Nat. Biotechnol.* **34**, 973–981 (2016).
21. Gut, G., Herrmann, M. D. & Pelkmans, L. Multiplexed protein maps link subcellular organization to cellular states. *Science (80-)* **361**, eaar7042 (2018).
22. Radtke, A. J. et al. IBEX: A versatile multiplex optical imaging approach for deep phenotyping and spatial analysis of cells in complex tissues. *Proc. Natl Acad. Sci. USA* **117**, 33455–33465 (2020).
23. Schubert, W. et al. Analyzing proteome topology and function by automated multidimensional fluorescence microscopy. *Nat. Biotechnol.* **24**, 1270–1278 (2006).
24. Jungmann, R. et al. Multiplexed 3D cellular super-resolution imaging with DNA-PAINT and Exchange-PAINT. *Nat. Methods* **11**, 313–318 (2014).
25. Saka, S. K. et al. Immuno-SABER enables highly multiplexed and amplified protein imaging in tissues. *Nat. Biotechnol.* **37**, 1080–1090 (2019).
26. Wichmann, J. & Hell, S. W. Breaking the diffraction resolution limit by stimulated emission: stimulated-emission-depletion fluorescence microscopy. *Opt. Lett.* **19**, 780–782 (1994).
27. Schermelleh, L. et al. Subdiffraction multicolor imaging of the nuclear periphery with 3D structured illumination microscopy. *Science (80-)* **320**, 1332–1336 (2008).
28. Huang, B., Wang, W., Bates, M. & Zhuang, X. Three-dimensional super-resolution imaging by stochastic optical reconstruction microscopy. *Science (80-)* **319**, 810–813 (2008).
29. Manley, S. et al. High-density mapping of single-molecule trajectories with photoactivated localization microscopy. *Nat. Methods* **5**, 155–157 (2008).
30. Wang, Y. et al. Rapid sequential in situ multiplexing with DNA exchange imaging in neuronal cells and tissues. *Nano Lett.* **17**, 6131–6139 (2017).
31. Jungmann, R. et al. Single-molecule kinetics and super-resolution microscopy by fluorescence imaging of transient binding on DNA origami. *Nano Lett.* **10**, 4756–4761 (2010).
32. Chung, K. K. H. et al. Fluorogenic DNA-PAINT for faster, low-background super-resolution imaging. *Nat. Methods* **19**, 554–559 (2022).
33. Schueder, F. et al. Multiplexed 3D super-resolution imaging of whole cells using spinning disk confocal microscopy and DNA-PAINT. *Nat. Commun.* **8**, 1–9 (2017).
34. Narayanasamy, K. K. et al. Visualizing synaptic multi-protein patterns of neuronal tissue with DNA-assisted single-molecule localization microscopy. *Front. Synaptic Neurosci.* **13**, 671288 (2021).
35. Klevanski, M. et al. Automated highly multiplexed super-resolution imaging of protein nano-architecture in cells and tissues. *Nat. Commun.* **11**, 1552 (2020).
36. Shi, L. et al. Super-resolution vibrational imaging using expansion stimulated raman scattering microscopy. *Adv. Sci.* **9**, e2200315 (2022).
37. Tavakoli, M. R. et al. Light-microscopy based dense connectomic reconstruction of mammalian brain tissue. *bioRxiv* https://doi.org/10.1101/2024.03.01.582884. (2024).
38. Yu, C. C. et al. Expansion microscopy of c. Elegans. *Elife* **9**, 1–78 (2020).
39. Bloom, G. S. Amyloid-β and tau: the trigger and bullet in alzheimer disease pathogenesis. *JAMA Neurol.* **71**, 505–508 (2014).
40. Tzioras, M., McGeachan, R. I., Durrant, C. S. & Spires-Jones, T. L. Synaptic degeneration in Alzheimer disease. *Nat. Rev. Neurol.* **19**, 19–38 (2022).
41. Pickett, E. K. et al. Non-fibrillar oligomeric amyloid-β within synapses. *J. Alzheimer's Dis.* **53**, 787–800 (2016).
42. Bayer, T. A. & Wirths, O. Intracellular accumulation of amyloid-beta - a predictor for synaptic dysfunction and neuron loss in Alzheimer's disease. *Front. Aging Neurosci.* **2**, 8 (2010).
43. Seo, J. et al. Activity-dependent p25 generation regulates synaptic plasticity and Aβ-induced cognitive impairment. *Cell* **157**, 486–498 (2014).
44. Zhao, W.-Q. et al. Inhibition of calcineurin-mediated endocytosis and alpha-amino-3-hydroxy-5-methyl-4-isoxazolepropionic acid (AMPA) receptors prevents amyloid beta oligomer-induced synaptic disruption. *J. Biol. Chem.* **285**, 7619–7632 (2010).
45. Zhang, Y. et al. Reduced levels of the tyrosine phosphatase STEP block β amyloid-mediated GluA1/GluA2 receptor internalization. *J. Neurochem.* **119**, 664–672 (2011).
46. Lima Caldeira, G., Peça, J. & Carvalho, A. L. New insights on synaptic dysfunction in neuropsychiatric disorders. *Curr. Opin. Neurobiol.* **57**, 62–70 (2019).
47. Koopmans, F. et al. SynGO: an evidence-based, expert-curated knowledge base for the synapse. *Neuron* **103**, 217–234.e4 (2019).
48. Klapoetke, N. C. et al. Independent optical excitation of distinct neural populations. *Nat. Methods* **11**, 338–346 (2014).
49. Seabold, S. & Perktold, J. Statsmodels: econometric and statistical modeling with python. *PROC. 9th PYTHON Sci. CONF* (2010).

Acknowledgements

We thank Daniel Goodwin, Yosuke Bando, and Atsushi Kajita for their help adapting the ExSeqProcessing registration pipeline for multiExR. We thank Dr. Li-Huei Tsai for the gift of 5xFAD mice and feedback on the manuscript. G.F. and J.K. were supported by the Tan-Yang Center for Autism Research at MIT. M.E.S was supported by the MathWorks Science Fellowship, the Collamore-Rogers Fellowship, the National Science Foundation Graduate Research Fellowship under Grant No. 1745302, and NIH 1F31MH133329-01. D.W. is supported by NSF IIS-2239688. E.N. is supported by the Alana Foundation USA, Halis Family Foundation, Lester A. Gimpelson, Donald and Glenda Mattes, David B. Emmes, and Thomas A. Stocky and Avni U. Shah. E.S.B. was supported by Tom Stocky, NIH 1R01EB024261, Kathleen Octavio, Lore McGovern, Good Ventures/Open Philanthopy, Lisa Yang, NIH 1R01AG070831, HHMI, the European Union's Horizon 2020 research and innovation programme (grant agreement No 835102), NIH 1R56AG069192, NIH R01MH124606, NIH R37MH080046, and John Doerr. The funders had no role in study design, data collection and analysis, decision to publish, or preparation of the manuscript.

Author contributions

J.K. contributed key ideas, designed and performed experiments and interpreted data for all projects, and wrote and edited the manuscript. M.E.S. contributed key ideas, designed experiments, designed and implemented analysis, visualization, and statistical tests for all projects, and wrote and edited the manuscript. E.S.B. supervised the project, initiated work, contributed key ideas, designed experiments, helped with data analysis and interpretation, and wrote and edited the manuscript. Y.L., E.Y., and K.T. performed data collection and wrote the methods. C.K. implemented the point-based registration method with extensive result analysis and wrote its description. T.B.T. aided with the design of nanoscale imaging of synaptic proteins and edited the manuscript. M.Z. provided mouse brain tissues and antibodies. D.P. provided cultured neurons. E.N. edited the 5xFAD-related parts in the manuscript. D.W. adapted the intensity-based registration method, supervised the development of the point-based registration method, and edited the registration method description. G.F. provided supervision and edited the manuscript.

Competing interests

J.K., M.E.S., and E.S.B. are co-inventors on a patent application for multiExR. The remaining authors declare no competing interests.

Additional information

Supplementary information The online version contains supplementary material available at https://doi.org/10.1038/s41467-024-53729-w.

Correspondence and requests for materials should be addressed to Edward S. Boyden.

Peer review information *Nature Communications* thanks Yiping Cui, and the other, anonymous, reviewer(s) for their contribution to the peer review of this work. A peer review file is available.

Supplementary Information

Multiplexed expansion revealing for imaging multiprotein nanostructures in healthy and diseased brain

Jinyoung Kang[1,2,*], Margaret E. Schroeder[1,3,*], Youngmi Lee[1], Chaitanya Kapoor[4], Eunah Yu[1], Tyler B. Tarr[5], Kat Titterton[1], Menglong Zeng[1], Demian Park[1], Emily Niederst[6], Donglai Wei[7], Guoping Feng[1,2,3,8], Edward S. Boyden[1,2,3,9,10,11,12,13**]

Contents

A. multiExR experiment planning decision tree

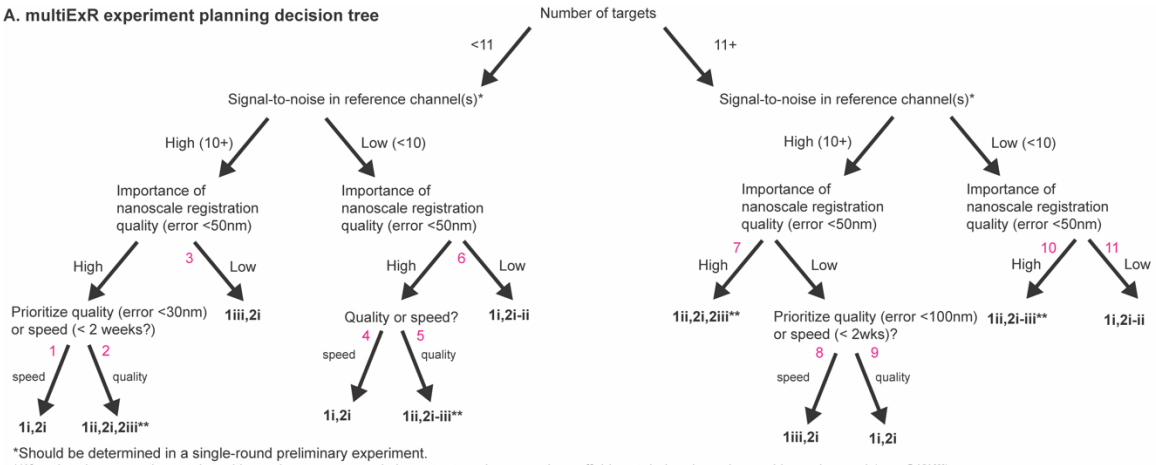

*Should be determined in a single-round preliminary experiment.
If registering synaptic proteins with maximum accuracy is important, and a synaptic scaffold protein has been imaged in each round (see **C(2)iii).

B. Simplified table for choosing reference channels

	i	ii	iii
# target proteins/round	2	1-2	3
average registration error	20-70nm	10-40nm	50-100nm
channel wavelengths (nm)	488/546: target proteins 633: multi-target reference	488 and/or 546: target protein(s), 594 Lectin + 633: synaptic protein reference	488/546/633: target proteins, 594 Lectin: reference

C. Legend and details

1. Reference channel
i. 3+ proteins in one reference channel (Figs. 3-5, Extended Data Figs. 2-4)
PROS: improved registration relative to (iii), usually in the 20-70nm range, more targets per round than (ii)
CONS: lower registration quality relative to (ii), 2 target proteins per round (multi-target reference cannot be in 594 nm channel, as bleedthrough is likely to overlap with target proteins in 546 and 633 nm channels)
ii. Multiple single-protein channels combined (normalized and summed) to a single reference channel (Fig. 2)
PROS: in our hands, consistently improved registration relative to (i), usually in the 10-40nm range, because relative intensities of each reference protein channel can be normalized
CONS: only 1-2 target channels can be imaged per round
iii. One single-protein as a single reference channel (e.g., Lectin stain in 594nm, used in earlier datasets not shown)
PROS: can allow 3 targets to be imaged per round (reference channel in 594nm, targets in 488nm, 546nm, and 633nm), if bleedthrough is unimportant (e.g., synaptic proteins being imaged with blood vessel as main feature in registration channel)
CONS: lower registration quality (usually in the 50-100nm range) and potential failures if reference channel protein is not dense (>3% of field of view by volume for a ~20um thick volume in physical units), bright (SNR > 10), and lacks features at multiple scales (by qualitative inspection)

2. Registration algorithm
i. Global feature-based (ExSeq Processing, Alon et al., Science 2021; Figs. 2-4, Extended Data Figs. 2-4)
PROS: fast (with GPU), and usually accurate within 50nm for reference channels with high signal-to-noise
CONS: slower (without GPU), high failure rate (>50%) for noisy reference channels (SNR < 10) if strategy 1(iii) is chosen
ii. Global intensity-based (Elastix, Klein et al., 2010; Extended Data Fig. 2, Fig. 5, Extended Data Fig. 4)
PROS: Can outperform (i) in cases where there is low staining intensity (SNR < 10)
CONS: Cannot run on GPU, subpar results when there are multiple structures e.g., neuronal processes due to global affine transformation, needs manual setting of multiple filtering parameters in case of noisy images
iii. Local point-based (Landmark-based RBF, Rohr et al., 2003; Extended Data Fig. 4)
PROS: capable of aligning "fine" structures e.g., synapses by computing a non-linear deformation field; can improve local registration quality of small, punctate nanostructures like synapses beyond (i) and (ii)
CONS: need to generate dense deformation field (same resolution as original image; high memory usage), cannot run on GPU, requires consistent nanostructure signal in each imaging round (e.g., similar synaptic markers), local deformation may disrupt global registration quality

Supplementary Figure 1. Guidelines for choosing multiExR reference channel(s) and registration method(s). A, Decision tree to help experimenters select a starting point for reference channel and registration algorithm based on experimental goals and practical constraints. Note that these choices can be further optimized based on the results of pilot experiments. Magenta numbers denote paths on the tree for easy reference in the text. Magenta numbers indicate paths on the decision tree, as referred to in the main text. **B**, Simplified table for choosing reference and registration channels. Average registration error ranges are an estimate. **I-iii** refer to the reference channel options detailed in **C**. **C**, Legend and details for (**A**) and (**B**), detailing the pros and cons of each (1) reference channel option and (2) registration algorithm option based on our experience. We do not provide a blanket recommended sequence for the staining of different targets. The prioritizing of protein targets in rounds may depend on the purpose of the study, the expression level of the protein targets, and the quality and host species of the antibodies. It may be helpful to image one or more structural/marker proteins in the earlier rounds to choose the most appropriate fields of view for imaging in later rounds. Additionally, low-expressing protein targets and/or

antibodies that yield low signal to noise might be better suited for earlier rounds, where the chance of signal degradation is lowest (although note the observation, in the main text, that some epitopes may benefit from an antigen retrieval effect of stripping), while high-expressing protein targets and/or antibodies that yield high signal to noise might be better suited for later rounds. Abbreviations: SNR, signal to noise ratio; GPU, graphics processing unit; RBF, radial basis function.

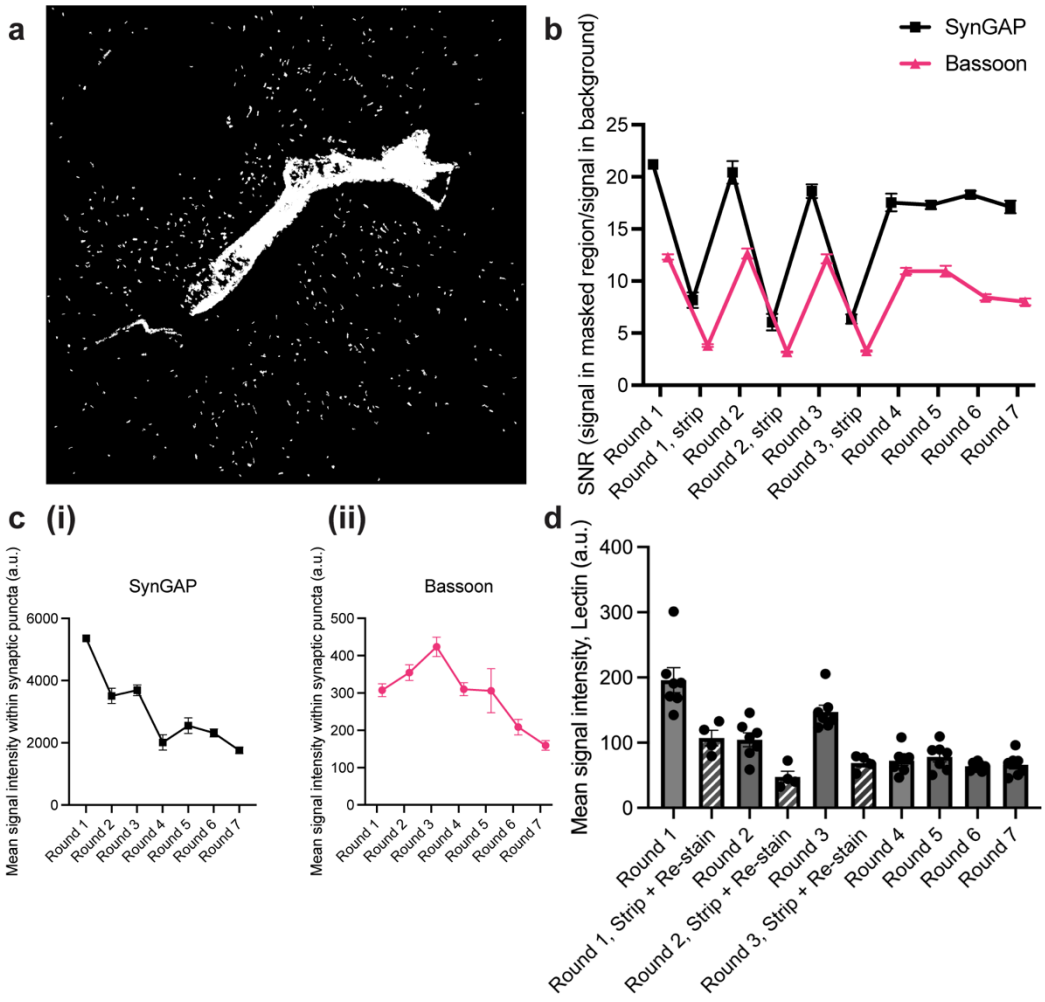

Supplementary Figure 2. Primary validation of stripping and re-staining efficiency with multiExR. **a,** The summed reference channel mask for **Fig. 2**, used to calculate the number of objects detected in the whole field of view. **b,** Signal-to-noise ratio, calculated as signal in masked region divided by signal in background, see **Methods**) of synaptic proteins within manually-identified synaptic ROIs for the primary validation dataset (n = 7 fields of view from one mouse, mean is taken over 51-53 ROIs per field of view). **c**, Mean signal intensity within synaptic puncta (masked) within manually-identified synaptic ROIs for the primary validation dataset for (i) SynGAP and (ii) Bassoon channels (n = 7 fields of view from one mouse, mean is taken over 51-53 ROIs per field of view). **d,** Mean fluorescence signal intensity in arbitrary units (a.u.) of the Lectin channel after several rounds of staining, stripping and re-staining (n = 7 fields of view from one mouse, mean is taken across the entire field of view). For population and comparative statistics, see **Supplementary Table 3.** Source data are provided as a Source Data file.

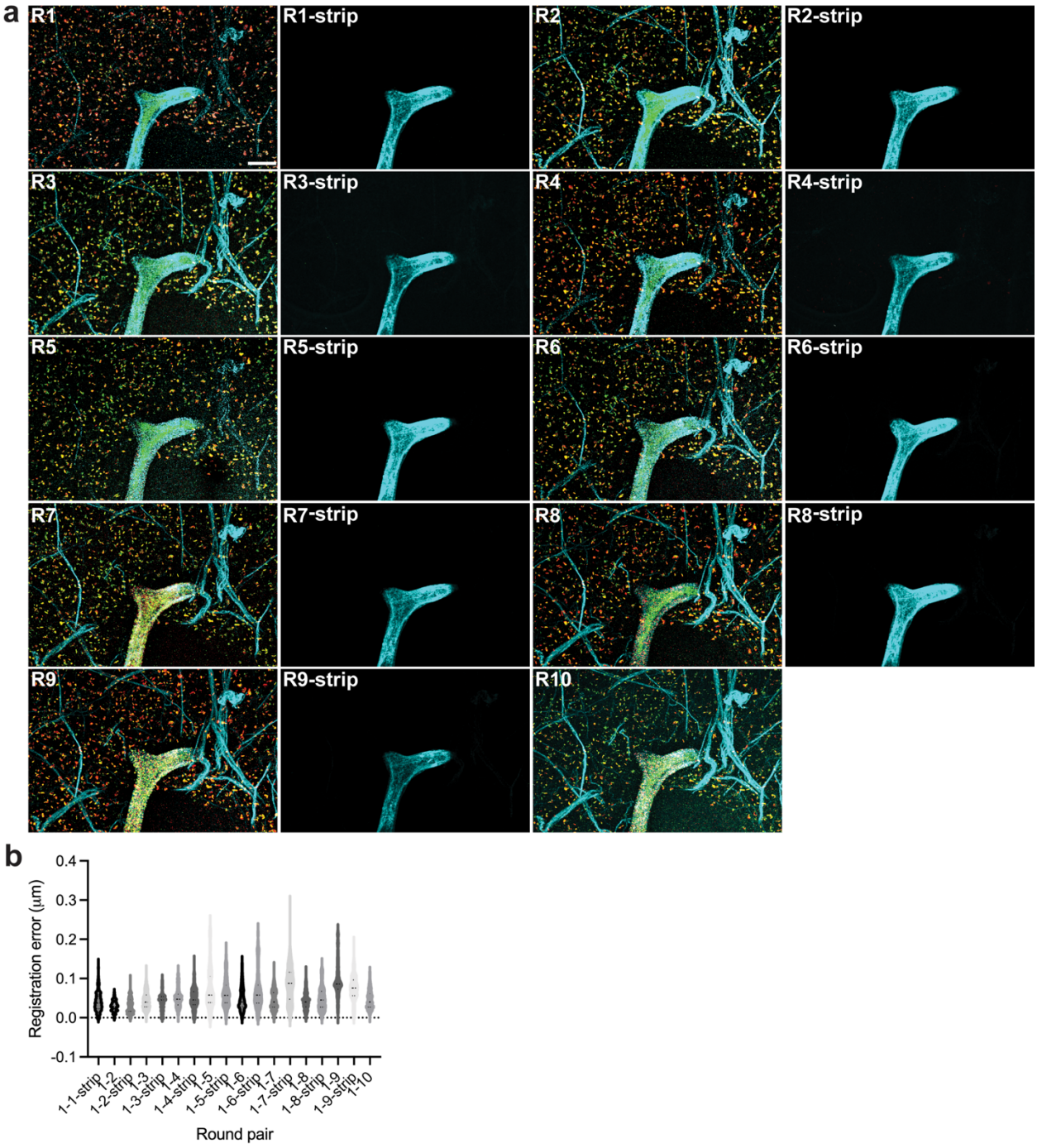

Supplementary Figure 3. Additional validation of stripping and re-staining efficiency with multiExR. a, Cropped maximum intensity projection for an example field of view from the registered secondary validation dataset, showing rounds 1-10 of staining and accompanying stripping rounds (red: SynGAP, green: NMDAR1, cyan: Lectin/SMI/GFAP/Homer reference channel). Pixel intensities are adjusted to the same minimum and maximum value for pairs of stripping and staining rounds. However, the min-max range is set differently for staining rounds imaged using different microscopes. Scale bar, 2 µm in biological units. **b**, Estimated population distribution (violin plot of density, with a dashed line at the median and dotted lines at the quartiles) of the registration error in an exemplary field of view from the secondary validation dataset (**a**), with the 95% confidence interval for each round pair tabulated below

(n = 924-990 randomly sampled subvolumes from one field of view from one mouse, see **Supplementary Table 4** for complete statistics). Source data are provided as a Source Data file.

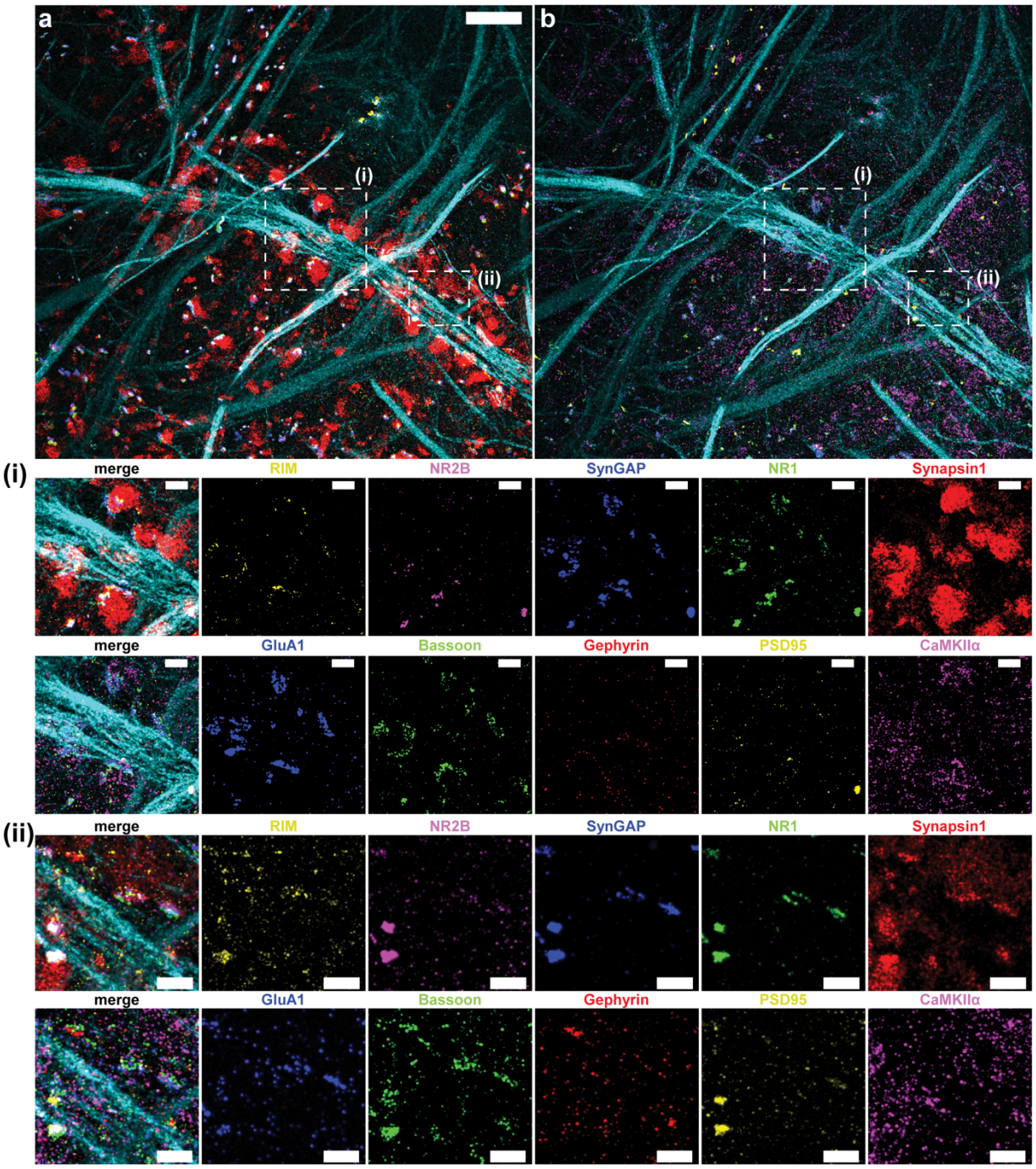

c

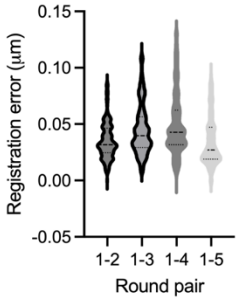

	1-2	1-3	1-4	1-5
Lower 95% CI of mean	0.03392	0.04364	0.04809	0.03304
Upper 95% CI of mean	0.03598	0.04645	0.05156	0.03566

Supplementary Figure 4. 10-plexed nanoscale characterization of putative synapses in cultured neurons. **a-b,** Composite 5-channel maximum intensity projection of a representative field of view of synaptic proteins in cultured hippocampal neurons obtained using multiExR. Scale bar, 2 μm in biological units. **a(i)-b(ii),** Single-channel and composite maximum intensity projections of synaptic proteins in the boxed regions from **(a)** and **(b)**. Scale bar, 500 nm in biological units **c,** Estimated population distribution (violin plot of density, with a dashed line at the median and dotted lines at the quartiles) of the registration error in a representative field of view, with the 95% confidence interval for each round pair tabulated below (see **Methods**, n = 870-1,000 randomly sampled subvolumes from one field of view from one batch of cultured neurons, see **Supplementary Table 13** for full statistics). Source data are provided as a Source Data file. This experiment was performed a single time and not repeated.

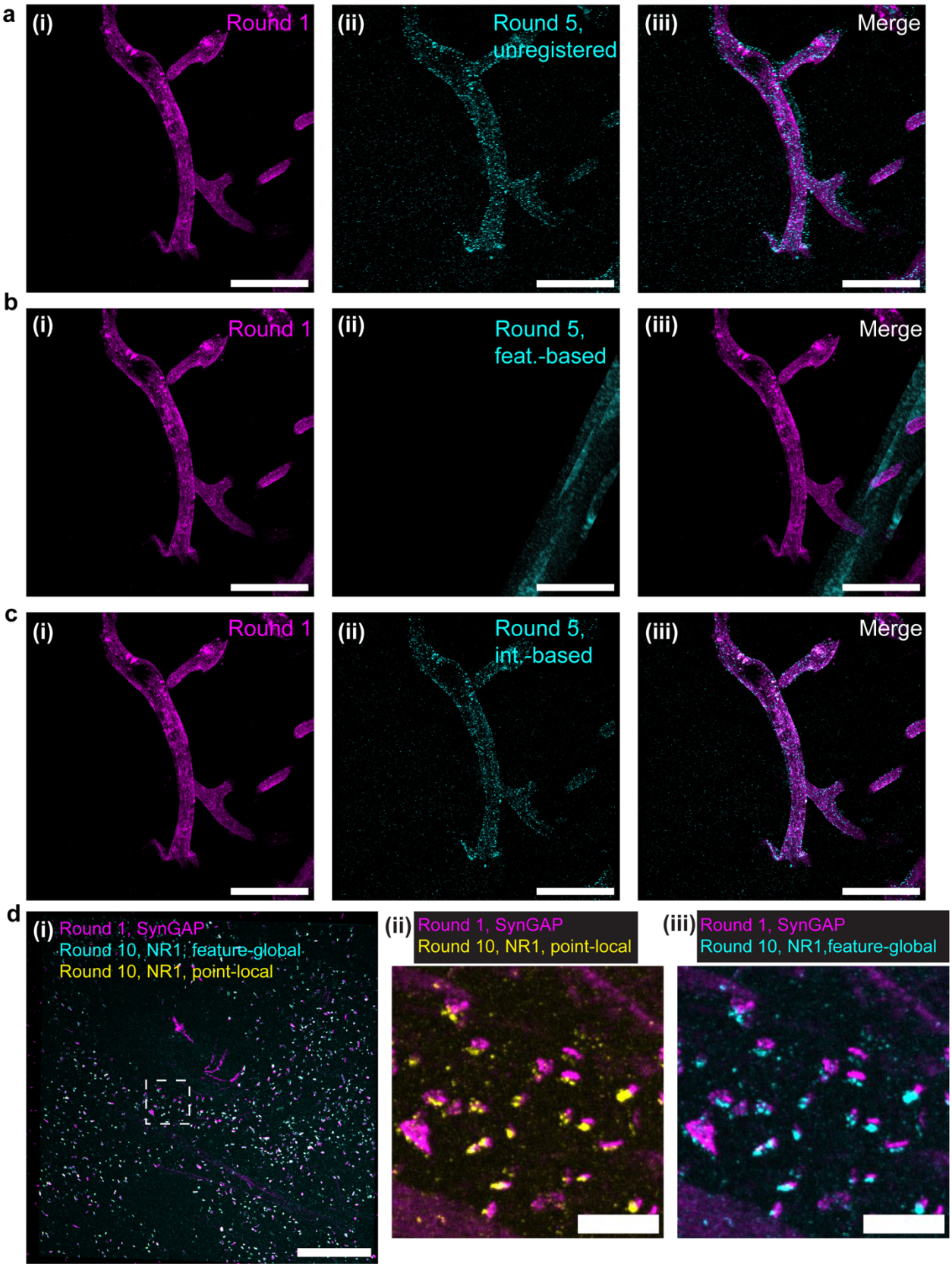
a
(i)
Round 1
(ii)
Round 5,
unregistered
(iii)
Merge
b
(i)
Round 1
(ii)
Round 5,
feat.-based
(iii)
Merge
c
(i)
Round 1
(ii)
Round 5,
int.-based
(iii)
Merge
d
(i) Round 1, SynGAP
Round 10, NR1, feature-global
Round 10, NR1, point-local
(ii) Round 1, SynGAP
Round 10, NR1, point-local
(iii) Round 1, SynGAP
Round 10, NR1,feature-global

Supplementary Figure 5. Example use cases of additional registration algorithms. **a(i)**, Maximum intensity projection (MIP) of first-round reference channel (Lectin) in the cortex of the 5xFAD mouse brain. **a(ii)**, MIP of the fifth-round reference channel (Lectin/SMI/GFAP), without registration. **a(iii)** Merged overlay of **(i)** and (**iii**). **b,** Same as **(a)**, for the fifth-round image volume registered using the global feature-based ExSeqProcessing registration algorithm (algorithm **2(i)** in **Supplementary Fig. 1C**). **c,** Same as **(a)**, for the fifth-round image volume registered using the global intensity-based registration algorithm (algorithm **2(ii)** in **Supplementary Fig. 1C**). **d(i),** MIP composite overlay of a first-round synaptic channel (SynGAP), a tenth-round synaptic channel (NR1) registered using the global feature-based ExSeqProcessing registration algorithm, and a tenth-round synaptic channel (NR1) registered using the global intensity-based algorithm (algorithm **2(ii)**) followed by the local point-based registration algorithm **2(iii)** in **Supplementary Fig. 1C**). **d(ii)** Zoom-in of the boxed region in **d(i)** showing the composite overlay of the first-round and tenth-round synaptic channels from the point-based local registration algorithm (algorithms **2(ii)** and **2(iii)** in **Supplementary Fig. 1C**). **d(iii)** Same as **d(ii)**, for the global feature-based ExSeqProcessing registration method (algorithm **2(i)** in **Supplementary Fig. 1C**).

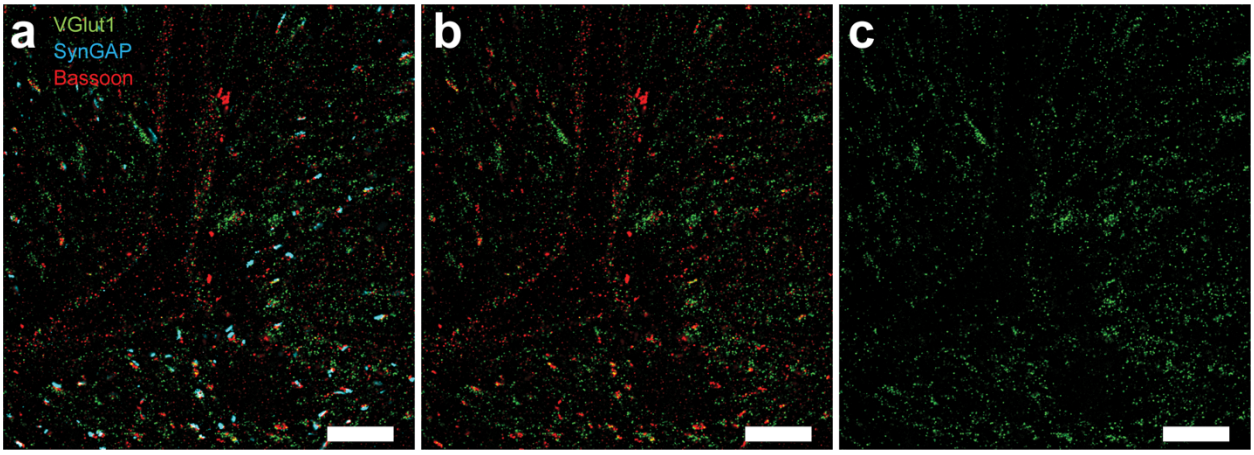

Supplementary Figure 6. A single z-plane of synaptic proteins showing colocalization of VGlut1, Bassoon, and SynGAP. Composite **(a)** 3-channel, **(b)** 2-channel, and **(c)** single channel of a representative field of view showing synaptic proteins in mouse somatosensory cortex obtained using multiExR (from one of two mice from one batch of experiments). Scale bar, 2 μm in biological units.

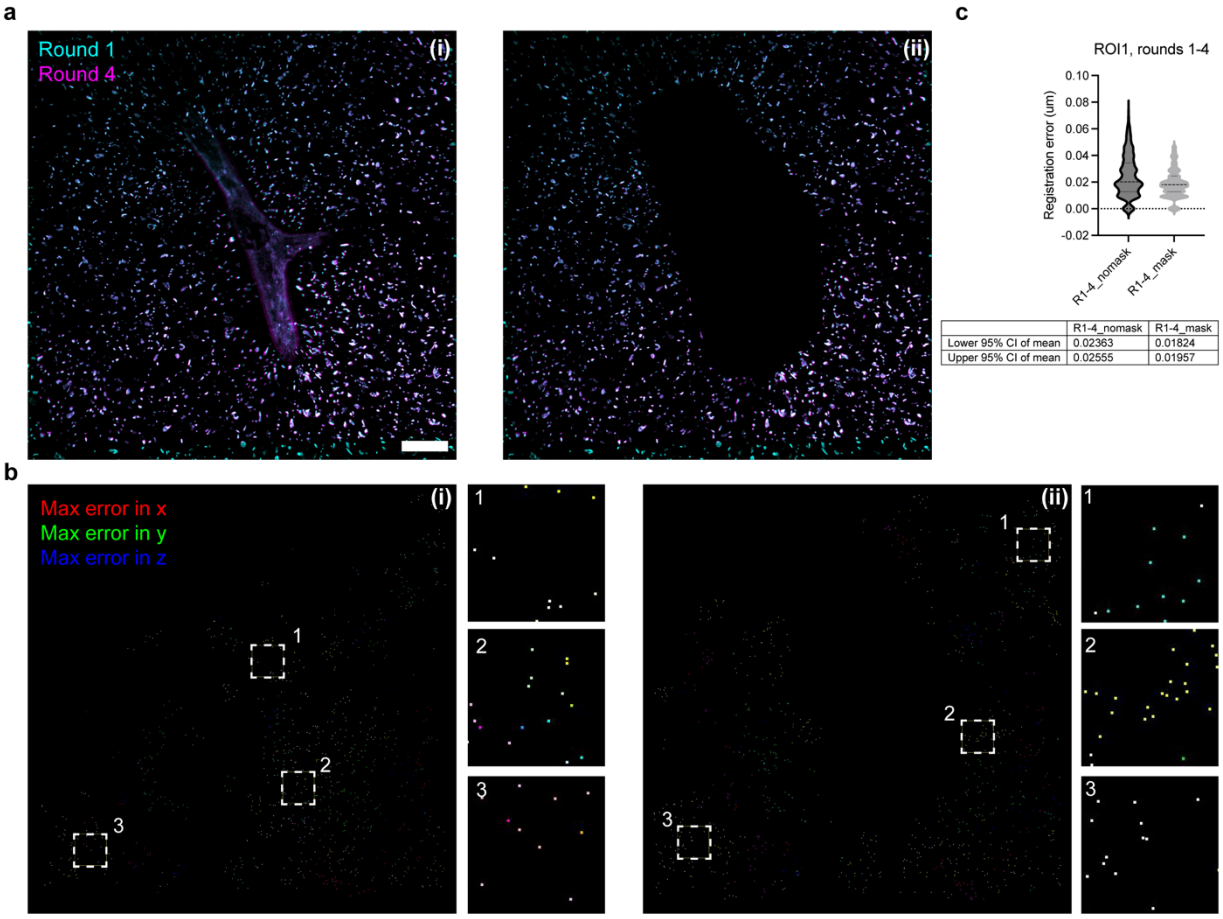

	R1-4_nomask	R1-4_mask
Lower 95% CI of mean	0.02363	0.01824
Upper 95% CI of mean	0.02555	0.01957

Supplementary Figure 7. Masking can improve registration error. a(i), Composite maximum intensity projection of the synGAP channel in imaging rounds 1 and 4 of the primary validation dataset, for the entire field of view whose registration error is shown in **Fig. 2f** (ROI1). **(ii)** Same as **(i)**, with a visually-determined higher-registration error area masked out. The mask was created and applied manually in Fiji using image math. **b(i),** RGB format maximum intensity projection of the same field of view as in **(a)**, with 100-voxel subvolumes colored by the maximum registration error (normalized to image maximum of 255) in x (red), y (green) and z (blue). To assist in visualization, the image was rescaled from 0 (minimum) to 30 (maximum) intensity, so that 30 became 255. **1-3)** Zoomed insets of the boxed regions in **(i)**. **(ii)** Same as **(i)**, with the higher-registration error area masked out. We qualitatively examined both the composite overlay of the synGAP channel (used to calculate registration error) and the RGB image showing the magnitude of the registration error in x, y, and z in red, green, and blue to identify the area of higher registration error in the x-y plane (note that the z-stack was already trimmed to the middle region, removing edges that are prone to registration offsets, see **Methods**). **c,** Estimated population distribution (violin plot of density, with a dashed line at the median and dotted lines at the quartiles) of the registration error in the unmasked, original field of view (dark gray) or the masked field of view (light gray), after outlier removal as described in the **Methods**. The 95% confidence interval of the mean registration error is provided below (n = 988 subvolumes for unmasked image after outlier removal, n = 966 subvolumes for masked image after outlier removal). Using this procedure, we were able to reduce the 95% confidence interval of the mean registration error (across subvolumes within each field of view) from 23.63-25.55nm to 18.24-19.57nm. Of note, the masked field of view retains ~80% of the original area in the x-y plane. In theory, the registration error range could be reduced even further by more aggressive cropping to even lower registration-error regions. Source data are provided as a Source Data file.

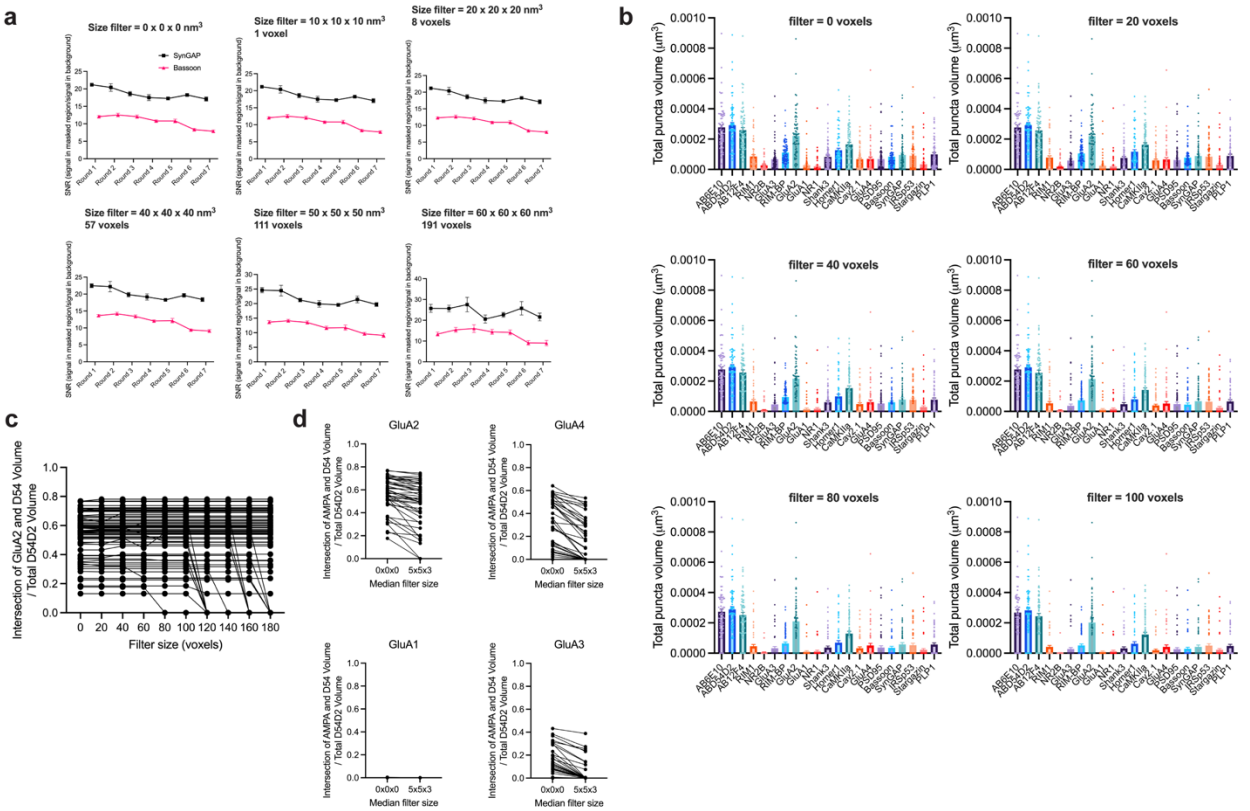

145

146 **Supplementary Figure 8.** Sensitivity of results to median and size filter sizes. **a,** Signal-to-noise ratio,
147 calculated as signal in masked region divided by signal in background (as in **Supplementary Fig. 2b**) of
148 synaptic proteins within manually-identified synaptic ROIs for the primary validation dataset with various
149 minimum size filters (n = 7 fields of view from one mouse, mean is taken over 51-53 ROIs per field of
150 view). **b,** Bar plots of total volume of select proteins within Aβ nanocluster ROIs (as in **Fig. 4b**, n = 71
151 ROIs from 9 fields of view from 2 5xFAD animals; error bars indicate mean +/- standard error of the
152 mean), with various minimum size filters. **c,** Fraction of volume of D54D2 occupied by AMPA receptor,
153 as in **Fig. 4c,** as a function of minimum filter size, where data points from the same nanocluster ROI are
154 connected by lines (n = 44 nanocluster ROIs from 8 fields of view from 2 5xFAD animals). **d**, Same as
155 **(c)**, but as a function of median filter size. Source data are provided as a Source Data file.

156

Supplementary Table 1. Mean feature density of masked binary reference channel (summed mask of each individual channel, which was used for registering this dataset), measured by volume, across 7 fields of view and 7 rounds in the primary validation dataset. Total feature volume is calculated as the sum of all nonzero pixels in the binary image (see **Methods**) across all channels. Largest feature volume is calculated as the mean number of nonzero pixels in the largest connected component across all channels, and smallest feature volume is calculated as the mean number of nonzero pixels in the smallest connected component across all channels. The mean was first taken across all rounds for each field of view, and then across all fields of view.

	Total feature volume / total image volume	Largest feature volume / total feature volume	Smallest feature volume / total feature volume
Mean	0.01256	0.4921	2.832×10^{-5}
95% CI	[0.01110,0.01402]	[0.3707,0.6136]	[2.368×10^{-5}, 3.297×10^{-5}]

Supplementary Table 2. Registration error for the primary validation dataset, measured using the SynGAP channel for the staining rounds, which was chosen based on its high signal-to-noise ratio across rounds, and the Lectin channel for the stripping rounds, which were re-stained for Lectin (**Fig. 2, Supplementary Fig. 2**).

Field of view name	**Round pair**	**# of ROIs after outlier removal**	**Mean (um)**	**Lower 95% of mean (um)**	**Upper 95% of mean (um)**
ROI1	1-2	989	0.01522	0.01467	0.01578
ROI1	1-3	995	0.02351	0.02271	0.0243
ROI1	1-4	990	0.02539	0.02443	0.02635
ROI1	1-5	972	0.02427	0.02337	0.02516
ROI1	1-6	951	0.02586	0.02491	0.02681
ROI1	1-7	974	0.02756	0.02657	0.02855
ROI2	1-2	985	0.01397	0.01342	0.01452
ROI2	1-3	993	0.02931	0.02835	0.03027
ROI2	1-4	945	0.0189	0.01822	0.01958
ROI2	1-5	970	0.02005	0.01916	0.02094
ROI2	1-6	937	0.02105	0.02017	0.02194
ROI2	1-7	921	0.02091	0.01999	0.02183
ROI3	1-2	1000	0.0323	0.03109	0.03351

ROI3	1-3	1000	0.04885	0.04708	0.05062
ROI3	1-4	993	0.05775	0.05543	0.06007
ROI3	1-5	992	0.05781	0.0559	0.05971
ROI3	1-6	972	0.07241	0.06934	0.07548
ROI3	1-7	959	0.07244	0.06937	0.07552
ROI4	1-2	911	0.09789	0.0938	0.102
ROI4	1-3	964	0.0176	0.01696	0.01825
ROI4	1-4	943	0.02024	0.01929	0.0212
ROI4	1-5	963	0.02192	0.02087	0.02296
ROI4	1-6	940	0.02061	0.01966	0.02157
ROI4	1-7	909	0.02081	0.02001	0.02162
ROI5	1-2	977	0.01802	0.01746	0.01857
ROI5	1-3	980	0.03114	0.02995	0.03233
ROI5	1-4	932	0.02154	0.02078	0.02231
ROI5	1-5	945	0.02512	0.02434	0.02589
ROI5	1-6	944	0.02584	0.02489	0.02679
ROI5	1-7	932	0.02733	0.02641	0.02825
ROI6	1-2	999	0.01785	0.01738	0.01833
ROI6	1-3	945	0.02045	0.01976	0.02114
ROI6	1-4	938	0.02037	0.01972	0.02102
ROI6	1-5	947	0.02624	0.02543	0.02705
ROI6	1-6	967	0.02613	0.02525	0.02701
ROI6	1-7	878	0.01903	0.0184	0.01967
ROI8	1-2	939	0.02022	0.01934	0.02109
ROI8	1-3	991	0.03711	0.03568	0.03855
ROI8	1-4	799	0.02052	0.0198	0.02123

ROI8	1-5	1000	0.03439	0.03348	0.0353
ROI8	1-6	977	0.05826	0.05597	0.06054
ROI8	1-7	997	0.06845	0.06556	0.07134
ROI3	1-1_strip	1000	0.04976	0.04842	0.05109
ROI3	1-2_strip	1000	0.05802	0.05623	0.05981
ROI3	1-3_strip	1000	0.07903	0.07684	0.08122
ROI4	1-1_strip	1000	0.01805	0.01731	0.01879
ROI4	1-2_strip	1000	0.03002	0.02882	0.03121
ROI4	1-3_strip	1000	0.03998	0.03860	0.04135
ROI6	1-1_strip	859	0.02969	0.02813	0.03125
ROI6	1-2_strip	992	0.02879	0.02789	0.02970
ROI6	1-3_strip	1000	0.03692	0.03550	0.03834
ROI8	1-1_strip	991	0.07627	0.07224	0.08029
ROI8	1-2_strip	930	0.05248	0.04966	0.05531
ROI8	1-3_strip	982	0.03743	0.03574	0.03913

Supplementary Table 3. Descriptive statistics and results of tests for statistical significance for the difference in mean signal intensity in the Lectin reference channel across staining and stripping rounds for the primary validation dataset (**Supplementary Fig. 2d**). Data are from 7 fields of view, 4 of which have were imaged after stripping the first 3 rounds, from one wild-type mouse.

i) Descriptive statistics for the mean signal intensity in the Lectin reference channel.

	Number of values	**Mean**	**Std. Deviation**	**Std. Error of Mean**	**Lower 95% CI of mean**	**Upper 95% CI of mean**
Round 1	7	196	50.65	19.14	149.1	242.8
Round 1, Strip + Restain	4	107	23.92	11.96	68.99	145.1
Round 2	7	104.4	28.31	10.7	78.19	130.6
Round 2, Strip + Restain	4	47.46	17.5	8.75	19.61	75.3
Round 3	7	147	27.89	10.54	121.2	172.8

Round 3, Strip + Restain	4	68.98	12.1	6.05	49.72	88.23
Round 4	7	72.54	19.71	7.451	54.31	90.77
Round 5	7	78.32	20.56	7.77	59.31	97.33
Round 6	7	63.93	6.494	2.454	57.92	69.93
Round 7	7	66.18	17.01	6.43	50.44	81.91

ii) Summary of mixed effects analysis, performed in GraphPad Prism. Mixed effects analysis was performed instead of one-way ANOVA because stripping rounds were not imaged for some fields of view, leading to missing data.

Fixed effect (type III)	**P value**	**P value summary**	**(P < 0.05)?**	**F (DFn, DFd)**
Treatment (between columns)	<0.0001	****	Yes	F (1.642, 8.209) = 49.88
Random effects	**SD**	**Variance**		
Individual (between rows)	19.8	391.9		
Residual	16.59	275.3		

iii) Tukey's multiple comparisons test following mixed effects analysis, performed in GraphPad Prism.

Tukey's multiple comparisons test	**Mean Diff.**	**95.00% CI of diff.**	**Summary**	**Adjusted P Value**
Round 1 vs. Round 1, Strip	88.91	-47.61 to 225.4	ns	0.1518
Round 1 vs. Round 2	91.58	37.73 to 145.4	**	0.0036
Round 1 vs. Round 2, Strip	148.5	2.307 to 294.7	*	0.0479
Round 1 vs. Round 3	48.92	-0.9132 to 98.76	ns	0.0542
Round 1 vs. Round 3, strip	127.0	-39.93 to 293.9	ns	0.1032
Round 1 vs. Round 4	123.4	67.83 to 179.0	***	0.0008
Round 1 vs. Round 5	117.6	55.57 to 179.7	**	0.0020
Round 1 vs. Round 6	132.0	50.49 to 213.6	**	0.0047
Round 1 vs. Round 7	129.8	66.69 to 192.9	**	0.0013
Round 1, Strip vs. Round 2	2.668	-29.54 to 34.88	ns	0.9993
Round 1, Strip vs. Round 2, Strip	59.59	-8.841 to 128.0	ns	0.0726
Round 1, Strip vs. Round 3	-39.99	-110.6 to 30.64	ns	0.2106
Round 1, Strip vs. Round 3, strip	38.07	-6.565 to 82.70	ns	0.0767
Round 1, Strip vs. Round 4	34.50	-12.88 to 81.88	ns	0.1153
Round 1, Strip vs. Round 5	28.73	-4.903 to 62.36	ns	0.0764
Round 1, Strip vs. Round 6	43.11	-10.57 to 96.80	ns	0.0897
Round 1, Strip vs. Round 7	40.87	6.766 to 74.97	*	0.0303
Round 2 vs. Round 2, Strip	56.92	-12.94 to 126.8	ns	0.0864
Round 2 vs. Round 3	-42.65	-74.01 to -11.30	*	0.0116
Round 2 vs. Round 3, strip	35.40	-26.05 to 96.84	ns	0.2025
Round 2 vs. Round 4	31.83	3.480 to 60.19	*	0.0296

Round 2 vs. Round 5	26.06	-14.07 to 66.18	ns	0.2526
Round 2 vs. Round 6	40.45	-0.05939 to 80.95	ns	0.0503
Round 2 vs. Round 7	38.20	0.5219 to 75.88	*	0.0471
Round 2, Strip vs. Round 3	-99.57	-164.0 to -35.10	*	0.0147
Round 2, Strip vs. Round 3, strip	-21.52	-82.76 to 39.72	ns	0.5213
Round 2, Strip vs. Round 4	-25.09	-66.87 to 16.70	ns	0.1842
Round 2, Strip vs. Round 5	-30.86	-82.70 to 20.98	ns	0.1878
Round 2, Strip vs. Round 6	-16.47	-64.16 to 31.22	ns	0.5347
Round 2, Strip vs. Round 7	-18.72	-59.46 to 22.02	ns	0.3274
Round 3 vs. Round 3, strip	78.05	-17.64 to 173.7	ns	0.0862
Round 3 vs. Round 4	74.49	45.09 to 103.9	***	0.0004
Round 3 vs. Round 5	68.71	30.37 to 107.1	**	0.0027
Round 3 vs. Round 6	83.10	40.11 to 126.1	**	0.0018
Round 3 vs. Round 7	80.85	47.06 to 114.6	***	0.0005
Round 3, strip vs. Round 4	-3.565	-54.68 to 47.55	ns	0.9998
Round 3, strip vs. Round 5	-9.340	-51.43 to 32.75	ns	0.8430
Round 3, strip vs. Round 6	5.049	-14.13 to 24.23	ns	0.7391
Round 3, strip vs. Round 7	2.801	-36.19 to 41.79	ns	0.9997
Round 4 vs. Round 5	-5.775	-23.59 to 12.04	ns	0.8586
Round 4 vs. Round 6	8.613	-19.26 to 36.49	ns	0.8841
Round 4 vs. Round 7	6.366	-8.215 to 20.95	ns	0.6239
Round 5 vs. Round 6	14.39	-15.15 to 43.92	ns	0.5158
Round 5 vs. Round 7	12.14	4.054 to 20.23	**	0.0070
Round 6 vs. Round 7	-2.248	-26.27 to 21.77	ns	>0.9999

Supplementary Table 4. Registration error for second validation dataset, measured using the reference channel (**Supplementary Fig. 3**). Registration error measured using the other channels (SynGAP, NMDAR1) was similar. We note that the first attempt at obtaining round009 failed to produce signal due to experimenter error (likely omission of an antibody); thus, the attempt was repeated and another round of stripping and staining obtained).

Field of view name	**Round pair**	**# of ROIs after outlier removal**	**Mean (um)**	**Lower 95% of mean (um)**	**Upper 95% of mean (um)**
ROI1	1-1-strip	990	0.04034	0.0388	0.04188
ROI1	1-2	986	0.02974	0.02889	0.03059
ROI1	1-2-strip	999	0.02973	0.02856	0.03089
ROI1	1-3	977	0.04413	0.04278	0.04549
ROI1	1-3-strip	992	0.03971	0.03839	0.04103
ROI1	1-4	977	0.05041	0.04898	0.05183
ROI1	1-4-strip	988	0.04952	0.04791	0.05112

ROI1	1-5	924	0.07256	0.06927	0.07585
ROI1	1-5-strip	994	0.06316	0.06103	0.06529
ROI1	1-6	932	0.04705	0.04521	0.04889
ROI1	1-6-strip	877	0.06912	0.06595	0.07229
ROI1	1-7	990	0.04464	0.04315	0.04612
ROI1	1-7-strip	999	0.08439	0.08158	0.0872
ROI1	1-8	969	0.04214	0.04083	0.04346
ROI1	1-8-strip	986	0.0493	0.04745	0.05115
ROI1	1-9	946	0.09552	0.09277	0.09827
ROI1	1-9-strip	987	0.0754	0.07346	0.07734
ROI1	1-10	980	0.04567	0.04423	0.0471
ROI2	1-1-strip	915	0.07328	0.07055	0.07601
ROI2	1-2	995	0.04697	0.04548	0.04846
ROI2	1-2-strip	966	0.1236	0.1186	0.1287
ROI2	1-3	988	0.04343	0.04186	0.045
ROI2	1-3-strip	1000	0.2629	0.2489	0.2769
ROI2	1-4	996	0.06795	0.06547	0.07043
ROI2	1-4-strip	948	0.1098	0.106	0.1137
ROI2	1-5	933	0.08648	0.08344	0.08953
ROI2	1-5-strip	913	0.1902	0.1826	0.1978
ROI2	1-6	949	0.08814	0.08433	0.09196
ROI2	1-6-strip	941	0.1225	0.1192	0.1258
ROI2	1-7	809	0.09866	0.09141	0.1059
ROI2	1-7-strip	948	0.1999	0.1928	0.2070
ROI2	1-8	939	0.05672	0.05433	0.05912
ROI2	1-8-strip	949	0.1515	0.1455	0.1575
ROI2	1-9	966	0.07434	0.07161	0.07706

ROI2	1-9-strip	951	0.2236	0.2154	0.2319
ROI2	1-10	970	0.07714	0.074	0.08029
ROI3	1-1-strip	955	0.02038	0.01947	0.0213
ROI3	1-2	997	0.02382	0.02262	0.02503
ROI3	1-2-strip	1000	0.03003	0.02894	0.03111
ROI3	1-3	993	0.06608	0.06422	0.06794
ROI3	1-3-strip	973	0.02478	0.02348	0.02607
ROI3	1-4	934	0.06436	0.06254	0.06618
ROI3	1-4-strip	730	0.04095	0.03841	0.04349
ROI3	1-5	867	0.1445	0.1398	0.1492
ROI3	1-5-strip	992	0.04866	0.04645	0.05086
ROI3	1-6	995	0.05271	0.04948	0.05594
ROI3	1-6-strip	998	0.05627	0.05417	0.05838
ROI3	1-7	955	0.09863	0.09451	0.1027
ROI3	1-7-strip	990	0.06217	0.05979	0.06455
ROI3	1-8	996	0.07545	0.07202	0.07889
ROI3	1-8-strip	931	0.04437	0.04235	0.04639
ROI3	1-9	996	0.0755	0.07191	0.07909
ROI3	1-9-strip	925	0.06714	0.06404	0.07024
ROI3	1-10	940	0.06936	0.06643	0.07229

Supplementary Table 5. Protein and channel information for each round of the multiplexed 5xFAD dataset (n = 2 mice per condition) (**Figs. 3-4**).

	ch1 (633)	**ch2 (546)**	**ch3 (488)**
Round 1	Lectin/SMI/GFAP	RIM	AB6E10
Round 2	Lectin/SMI/GFAP	NR2B	GluA3
Round 3	Lectin/SMI/GFAP	RIM-BP	GluA2

Round 4	Lectin/SMI/GFAP	GluA1	NR1
Round 5	Lectin/SMI/GFAP	PLP1	Shank3
Round 6	Lectin/SMI/GFAP	Homer1	CaMKII
Round 7	Lectin/SMI/GFAP	D54D2	Cav2.1
Round 8	Lectin/SMI/GFAP	GluA4	12F4
Round 9	Lectin/SMI/GFAP	PSD95	Bassoon
Round 10	Lectin/SMI/GFAP	SynGAP	IRsp53
Round 11	Lectin/SMI/GFAP	Stargazin	Gephyrin*

*Excluded due to poor staining quality.

Supplementary Table 6. Registration error for the multiplexed 5xFAD vs. WT mouse dataset (n = 2 mice per condition), measured using the combined reference channel (**Figs. 3-4**).

Field of view name	**Round pair**	**# of subvolumes after outlier removal**	**Mean (um)**	**Lower 95% CI (um)**	**Upper 95% CI (um)**
S1ROI1 (5xFAD)	1-2	1000	0.05357	0.05184	0.05529
S1ROI1 (5xFAD)	1-3	1000	0.06229	0.0601	0.06449
S1ROI1 (5xFAD)	1-4	1000	0.088	0.08523	0.09077
S1ROI1 (5xFAD)	1-5	998	0.09537	0.09192	0.09882
S1ROI1 (5xFAD)	1-6	991	0.1052	0.1013	0.1091
S1ROI1 (5xFAD)	1-7	973	0.1047	0.1003	0.1091
S1ROI1 (5xFAD)	1-8	988	0.1507	0.1445	0.1568
S1ROI1 (5xFAD)	1-9	967	0.1477	0.1419	0.1536
S1ROI1 (5xFAD)	1-10	889	0.1251	0.1191	0.1311
S1ROI1 (5xFAD)	1-11	969	0.1503	0.1433	0.1574
S1ROI2 (5xFAD)	1-2	1000	0.02343	0.02258	0.02428
S1ROI2 (5xFAD)	1-3	1000	0.02922	0.02817	0.03026
S1ROI2 (5xFAD)	1-4	1000	0.03536	0.03402	0.03669

S1ROI2 (5xFAD)	1-5	1000	0.0405	0.03892	0.04208
S1ROI2 (5xFAD)	1-6	998	0.03929	0.03752	0.04106
S1ROI2 (5xFAD)	1-7	999	0.04371	0.0418	0.04562
S1ROI2 (5xFAD)	1-8	1000	0.04854	0.04642	0.05065
S1ROI2 (5xFAD)	1-9	1000	0.04845	0.04599	0.05091
S1ROI2 (5xFAD)	1-10	959	0.09445	0.09148	0.09743
S1ROI2 (5xFAD)	1-11	999	0.05537	0.05312	0.05762
S1ROI3 (5xFAD)	1-2	998	0.0138	0.01311	0.01448
S1ROI3 (5xFAD)	1-3	1000	0.01228	0.01166	0.0129
S1ROI3 (5xFAD)	1-4	975	0.02152	0.02072	0.02232
S1ROI3 (5xFAD)	1-5	1000	0.01882	0.01787	0.01976
S1ROI3 (5xFAD)	1-6	991	0.0241	0.02296	0.02525
S1ROI3 (5xFAD)	1-7	760	0.006232	0.00568	0.006783
S1ROI3 (5xFAD)	1-8	994	0.02094	0.01983	0.02204
S1ROI3 (5xFAD)	1-9	982	0.02181	0.02059	0.02304
S1ROI3 (5xFAD)	1-10	839	0.01284	0.01188	0.0138
S1ROI3 (5xFAD)	1-11	994	0.02612	0.02493	0.02731
S1ROI4 (5xFAD)	1-2	998	0.03358	0.03166	0.03549
S1ROI4 (5xFAD)	1-3	815	0.02288	0.02151	0.02426
S1ROI4 (5xFAD)	1-4	995	0.06163	0.05836	0.0649
S1ROI4 (5xFAD)	1-5	749	0.02593	0.02477	0.02708
S1ROI4 (5xFAD)	1-6	761	0.02315	0.022	0.0243
S1ROI4 (5xFAD)	1-7	787	0.02676	0.02544	0.02807
S1ROI4 (5xFAD)	1-8	777	0.02663	0.02533	0.02792
S1ROI4 (5xFAD)	1-9	778	0.03155	0.03029	0.03281
S1ROI4 (5xFAD)	1-10	768	0.03991	0.03767	0.04215
S1ROI4 (5xFAD)	1-11	797	0.0409	0.03895	0.04286

S1ROI5 (5xFAD)	1-2	1000	0.04371	0.04268	0.04475
S1ROI5 (5xFAD)	1-3	1000	0.04652	0.04512	0.04792
S1ROI5 (5xFAD)	1-4	1000	0.06155	0.05983	0.06326
S1ROI5 (5xFAD)	1-5	1000	0.06824	0.06608	0.0704
S1ROI5 (5xFAD)	1-6	1000	0.07194	0.06977	0.0741
S1ROI5 (5xFAD)	1-7	998	0.0833	0.0809	0.08569
S1ROI5 (5xFAD)	1-8	999	0.08965	0.08635	0.09295
S1ROI5 (5xFAD)	1-9	991	0.1011	0.09778	0.1045
S1ROI5 (5xFAD)	1-10	988	0.09982	0.09654	0.1031
S1ROI5 (5xFAD)	1-11	995	0.1024	0.09895	0.1058
S2ROI1 (5xFAD)	1-2	0.0233	0.02257	0.02404	1000
S2ROI1 (5xFAD)	1-3	0.02564	0.02473	0.02656	1000
S2ROI1 (5xFAD)	1-4	0.03254	0.03133	0.03375	1000
S2ROI1 (5xFAD)	1-5	0.03394	0.03262	0.03525	1000
S2ROI1 (5xFAD)	1-6	0.03902	0.0376	0.04045	1000
S2ROI1 (5xFAD)	1-7	0.04912	0.04729	0.05095	1000
S2ROI1 (5xFAD)	1-8	0.04632	0.04456	0.04807	1000
S2ROI1 (5xFAD)	1-9	0.05088	0.04894	0.05281	1000
S2ROI1 (5xFAD)	1-10	0.05191	0.04976	0.05407	1000
S2ROI1 (5xFAD)	1-11	0.06204	0.05985	0.06422	1000
S2ROI2 (5xFAD)	1-2	0.01522	0.0147	0.01573	913
S2ROI2 (5xFAD)	1-3	0.02099	0.01989	0.02208	1000
S2ROI2 (5xFAD)	1-4	0.02614	0.02515	0.02713	939
S2ROI2 (5xFAD)	1-5	0.02547	0.02438	0.02655	938
S2ROI2 (5xFAD)	1-6	0.03137	0.02994	0.0328	934
S2ROI2 (5xFAD)	1-7	0.02583	0.02433	0.02734	921
S2ROI2 (5xFAD)	1-8	0.04117	0.03896	0.04338	977

S2ROI2 (5xFAD)	1-9	0.03847	0.03647	0.04047	971
S2ROI2 (5xFAD)	1-10	0.03335	0.03144	0.03526	915
S2ROI2 (5xFAD)	1-11	0.04357	0.04153	0.04561	951
S2ROI3 (5xFAD)	1-2	0.01803	0.01722	0.01883	977
S2ROI3 (5xFAD)	1-3	0.02098	0.02013	0.02183	923
S2ROI3 (5xFAD)	1-4	0.02133	0.02041	0.02225	917
S2ROI3 (5xFAD)	1-5	0.02656	0.02537	0.02775	992
S2ROI3 (5xFAD)	1-6	0.02985	0.02863	0.03107	991
S2ROI3 (5xFAD)	1-7	0.02725	0.02599	0.02852	898
S2ROI3 (5xFAD)	1-8	0.02217	0.02133	0.023	883
S2ROI3 (5xFAD)	1-9	0.03627	0.03458	0.03796	942
S2ROI3 (5xFAD)	1-10	0.03572	0.03418	0.03725	934
S2ROI3 (5xFAD)	1-11	0.03977	0.0378	0.04174	954
S2ROI4 (5xFAD)	1-2	0.03583	0.03469	0.03698	979
S2ROI4 (5xFAD)	1-3	0.04729	0.04588	0.0487	1000
S2ROI4 (5xFAD)	1-4	0.0696	0.06738	0.07183	981
S2ROI4 (5xFAD)	1-5	0.07327	0.07153	0.07501	928
S2ROI4 (5xFAD)	1-6	0.08729	0.08485	0.08972	992
S2ROI4 (5xFAD)	1-7	0.1002	0.09772	0.1027	997
S2ROI4 (5xFAD)	1-8	0.1175	0.114	0.121	991
S2ROI4 (5xFAD)	1-9	0.1238	0.1202	0.1273	944
S2ROI4 (5xFAD)	1-10	0.1023	0.1001	0.1045	914
S2ROI4 (5xFAD)	1-11	0.1292	0.1262	0.1323	998
S3ROI1 (WT)	1-2	0.04098	0.03906	0.04289	998
S3ROI1 (WT)	1-3	0.02568	0.02481	0.02656	995
S3ROI1 (WT)	1-4	0.01959	0.01892	0.02027	972
S3ROI1 (WT)	1-5	0.02696	0.02616	0.02776	995

S3ROI1 (WT)	1-6	0.05027	0.04846	0.05207	1000
S3ROI1 (WT)	1-7	0.05638	0.05437	0.05839	1000
S3ROI1 (WT)	1-8	0.04515	0.04402	0.04627	996
S3ROI1 (WT)	1-9	0.04669	0.04527	0.04811	999
S3ROI1 (WT)	1-10	0.05092	0.04931	0.05253	1000
S3ROI1 (WT)	1-11	0.0459	0.04474	0.04705	998
S3ROI2 (WT)	1-2	0.01304	0.01264	0.01344	990
S3ROI2 (WT)	1-3	0.01944	0.01881	0.02007	1000
S3ROI2 (WT)	1-4	0.02082	0.02033	0.02131	1000
S3ROI2 (WT)	1-5	0.01391	0.01345	0.01437	951
S3ROI2 (WT)	1-6	0.02173	0.02107	0.02238	999
S3ROI2 (WT)	1-7	0.03299	0.03202	0.03397	993
S3ROI2 (WT)	1-8	0.02239	0.02163	0.02315	1000
S3ROI2 (WT)	1-9	0.01558	0.01505	0.01611	879
S3ROI2 (WT)	1-10	0.03076	0.02979	0.03172	1000
S3ROI2 (WT)	1-11	0.01898	0.01835	0.01961	995
S3ROI3 (WT)	1-2	0.01005	0.009553	0.01054	1000
S3ROI3 (WT)	1-3	0.0161	0.01559	0.0166	996
S3ROI3 (WT)	1-4	0.01443	0.01382	0.01503	1000
S3ROI3 (WT)	1-5	0.02465	0.02398	0.02532	995
S3ROI3 (WT)	1-6	0.01783	0.01707	0.01858	1000
S3ROI3 (WT)	1-7	0.0291	0.02826	0.02993	981
S3ROI3 (WT)	1-8	0.03132	0.03026	0.03238	1000
S3ROI3 (WT)	1-9	0.02515	0.02432	0.02599	979
S3ROI3 (WT)	1-10	0.02341	0.02252	0.0243	967
S3ROI3 (WT)	1-11	0.03025	0.02941	0.03109	984
S3ROI4 (WT)	1-2	0.01448	0.01405	0.01491	979

S3ROI4 (WT)	1-3	0.01397	0.01331	0.01462	1000
S3ROI4 (WT)	1-4	0.02117	0.02035	0.02199	972
S3ROI4 (WT)	1-5	0.01439	0.01378	0.01501	975
S3ROI4 (WT)	1-6	0.0187	0.01791	0.01949	990
S3ROI4 (WT)	1-7	0.01555	0.01503	0.01608	847
S3ROI4 (WT)	1-8	0.01877	0.01788	0.01965	972
S3ROI4 (WT)	1-9	0.01853	0.01778	0.01928	973
S3ROI4 (WT)	1-10	0.02762	0.02669	0.02855	949
S3ROI4 (WT)	1-11	0.01988	0.01908	0.02068	951
S4ROI1 (WT)	1-2	0.02937	0.02862	0.03013	994
S4ROI1 (WT)	1-3	0.04884	0.0473	0.05038	976
S4ROI1 (WT)	1-4	0.04548	0.04393	0.04703	1000
S4ROI1 (WT)	1-5	0.0443	0.04287	0.04572	1000
S4ROI1 (WT)	1-6	0.04846	0.04697	0.04995	1000
S4ROI1 (WT)	1-7	0.05113	0.04914	0.05311	1000
S4ROI1 (WT)	1-8	0.06986	0.06773	0.07198	1000
S4ROI1 (WT)	1-9	0.06512	0.06304	0.06721	997
S4ROI1 (WT)	1-10	0.07089	0.06835	0.07343	982
S4ROI1 (WT)	1-11	0.07369	0.07111	0.07628	996
S4ROI2 (WT)	1-2	0.02356	0.02282	0.02431	1000
S4ROI2 (WT)	1-3	0.03513	0.03394	0.03632	999
S4ROI2 (WT)	1-4	0.03518	0.03382	0.03653	998
S4ROI2 (WT)	1-5	0.04005	0.03866	0.04145	999
S4ROI2 (WT)	1-6	0.04043	0.039	0.04186	998
S4ROI2 (WT)	1-7	0.05032	0.04826	0.05238	993
S4ROI2 (WT)	1-8	0.0526	0.05048	0.05471	999
S4ROI2 (WT)	1-9	0.05509	0.05285	0.05732	995

S4ROI2 (WT)	1-10	0.06117	0.0585	0.06383	995
S4ROI2 (WT)	1-11	0.05886	0.0564	0.06133	998
S4ROI3 (WT)	1-2	0.03682	0.03558	0.03807	1000
S4ROI3 (WT)	1-3	0.04038	0.03908	0.04168	1000
S4ROI3 (WT)	1-4	0.04308	0.04154	0.04462	995
S4ROI3 (WT)	1-5	0.04911	0.04741	0.05082	1000
S4ROI3 (WT)	1-6	0.04884	0.04671	0.05096	994
S4ROI3 (WT)	1-7	0.05744	0.05534	0.05954	995
S4ROI3 (WT)	1-8	0.07016	0.06796	0.07235	994
S4ROI3 (WT)	1-9	0.07449	0.07166	0.07732	996
S4ROI3 (WT)	1-10	0.07017	0.06755	0.0728	990
S4ROI3 (WT)	1-11	0.07374	0.07071	0.07678	972
S4ROI4 (WT)	1-2	0.009341	0.008858	0.009825	999
S4ROI4 (WT)	1-3	0.0107	0.01005	0.01135	994
S4ROI4 (WT)	1-4	0.01402	0.01325	0.01479	1000
S4ROI4 (WT)	1-5	0.01694	0.01613	0.01775	1000
S4ROI4 (WT)	1-6	0.01674	0.01603	0.01745	996
S4ROI4 (WT)	1-7	0.01232	0.0115	0.01313	968
S4ROI4 (WT)	1-8	0.02091	0.01986	0.02196	999
S4ROI4 (WT)	1-9	0.02	0.01898	0.02101	989
S4ROI4 (WT)	1-10	0.02116	0.0201	0.02222	993
S4ROI4 (WT)	1-11	0.02132	0.02029	0.02235	999

Supplementary Table 7. Results of linear mixed effect model, implement in Python's statsmodels package[1], testing the effect of group (5xFAD vs. WT) on total volume of each synaptic protein, with group assignment equal to animal (n = 2 animals per group, n = 4-5 fields of view per animal).

Protein	**Group coefficient (WT)**	**Group z statistic**	**Group p-value**
RIM1	0.213	0.841	0.401

NR2B	0.121	4.801	1.58×10^{-6}
GluA3	0.161	4.705	2.54×10^{-6}
RIM-BP	0.199	2.245	0.025
GluA2	-0.029	-3.622	2.92×10^{-4}
GluA1	0.127	4.713	2.439×10^{-8}
NR1	0.142	4.836	1.327×10^{-6}
Shank3	0.248	3.412	6.438×10^{-4}
Homer1	0.124	1.865	0.062
CaMKIIa	-0.057	0.5885	-0.541
Cav2.1	0.155	0.00195	3.098
GluA4	-0.052	-1.438	0.1504
PSD95	0.321	3.441	5.803×10^{-4}
Bassoon	0.307	5.431	5.615×10^{-8}
SynGAP	0.336	7.699	1.372×10^{-14}
IRsp53	0.097	1.851	0.0642
Stargazin	0.096	0.1730	1.363

Supplementary Table 8. Descriptive statistics of Aβ, myelin, and synaptic protein volume within manually-identified Aβ nanocluster ROIs (**Fig. 4b**). Data are from 71 nanocluster ROIs from 9 fields of view from 2 12-month 5xFAD mice.

Protein	**Mean volume (um^3)**	**Lower 95% CI (um^3)**	**Upper 95% CI (um^3)**
6E10	0.0002773	0.0002427	0.0003118
D54D2	0.0002918	0.000257	0.0003266
12F4	0.000258	0.000224	0.0002921
RIM1	7.82E-05	5.55E-05	0.000101
NR2B	1.80E-05	1.07E-05	2.53E-05
GluA3	5.89E-05	3.79E-05	7.98E-05
RIM-BP	0.0001055	8.82E-05	0.0001229
GluA2	0.0002211	0.0001851	0.0002571
GluA1	2.35E-05	1.12E-05	3.59E-05

NR1	1.93E-05	5.67E-06	3.30E-05
Shank3	7.57E-05	5.66E-05	9.49E-05
Homer1	0.0001175	9.16E-05	0.0001434
CaMKIIa	0.0001625	0.0001347	0.0001903
Cav2.1	5.99E-05	4.33E-05	7.66E-05
GluA4	6.62E-05	4.02E-05	9.21E-05
PSD95	6.32E-05	4.16E-05	8.48E-05
Bassoon	7.78E-05	5.93E-05	9.64E-05
SynGAP	8.87E-05	6.35E-05	0.0001138
IRSp53	8.44E-05	6.14E-05	0.0001074
Stargazin	3.12E-05	1.40E-05	4.84E-05
PLP1	8.91E-05	6.56E-05	0.0001126

Supplementary Table 9. Statistics accompanying the analysis of GluA1-4 colocalization with D54D2 within manually-identified Aβ nanocluster ROIs (**Fig. 4c-e**). Analysis was conducted in GraphPad Prism.

i) Descriptive statistics of the fraction of volume mutually overlapped with D54D2 (e.g., GluA2 volume overlapped with D54D2 divided by total D54D2 volume, **Fig. 4c**) for all AMPAR subunits. Only ROIs with nonzero volumes of each protein after size filtration are included. For this analysis, we excluded ROIs with visible offset between the Aβ channels, representing residual registration error.

	GluA2	**GluA4**	**GluA3**	**GluA1**
Number of values	44	44	44	44
Mean	0.4835	0.1460	0.04257	0.000
Std. Deviation	0.1983	0.1828	0.09443	0.000
Std. Error of Mean	0.02990	0.02756	0.01424	0.000
Lower 95% CI of mean	0.4232	0.09042	0.01386	0.000
Upper 95% CI of mean	0.5438	0.2016	0.07128	0.000

ii) Results of one-way ANOVA followed by Tukey's multiple comparisons test on the fraction of volume mutually overlapped with D54D2 for all AMPAR subunits. Only ROIs with nonzero volumes of each protein after size filtration are included. For this analysis, we excluded ROIs with visible offset between the Aβ channels, representing residual registration error.

ANOVA table	**SS**	**DF**	**MS**	**F (DFn, DFd)**	**P value**
Treatment (between columns)	6.336	3	2.112	F(3, 172) = 103.4	P<0.0001

Residual (within columns)	3.512	172	0.02042		
Total	9.848	175			

Tukey's multiple comparisons test	Mean Diff.	95.00% CI of diff.	Below threshold?	Summary	Adjusted P Value
GluA1 vs. GluA2	0.3376	0.2585 to 0.4166	Yes	****	<0.0001
GluA1 vs. GluA3	0.4410	0.3619 to 0.5200	Yes	****	<0.0001
GluA1 vs. GluA4	0.4835	0.4045 to 0.5626	Yes	****	<0.0001
GluA2 vs. GluA3	0.1034	0.02439 to 0.1825	Yes	**	0.0047
GluA2 vs. GluA4	0.1460	0.06696 to 0.2250	Yes	****	<0.0001
GluA3 vs. GluA4	0.04257	-0.03646 to 0.1216	No	ns	0.5027

iii) Results of simple linear regression on the volume of GluA4 or GluA2 vs. D54D2 (**Fig. 4d**).

	GluA2	GluA4
Number of Values	71	71
Slope, 95% CI	[0.8456,1.046]	[0.3878,0.6465]
R squared	0.8370	0.4796
F	354.3	63.59
P value	<0.0001	<0.0001
Deviation from zero?	Significant	Significant

iv) Results of simple linear regression on the volume of GluA2 vs. GluA4 (**Fig. 4e**).

95% CI of slope	[0.8787, 1.292]
R^2	0.6143
P value	<0.0001
# of values	71

Supplementary Table 10. Protein and channel information for each round of multiplexed synaptic dataset (**Fig. 5)**, mice #1 (S1) and #2 (S2).

	ch1 (633)	ch2 (546)	ch3 (488)
Round 1	Lectin/SMI/GFAP	SynGAP	NR1
Round 2	Lectin/SMI/GFAP	RIM1	Gephyrin
Round 3	Lectin/SMI/GFAP	GluA4	IRSp53

Round 4	Lectin/SMI/GFAP	GluA1	NR2B
Round 5	Lectin/SMI/GFAP	Homer1	CaMKIIa
Round 6	Lectin/SMI/GFAP	*no signal	Shank3
Round 7	Lectin/SMI/GFAP	GluA3	Bassoon
Round 8	Lectin/SMI/GFAP	Erbb4	Stargazin
Round 9	Lectin/SMI/GFAP	Elfn1	no signal*
Round 10	Lectin/SMI/GFAP	PSD95	Cav2.1
Round 11	Lectin/SMI/GFAP	GluA2	Vglut1

*Excluded from analysis and visualization due to poor staining quality or were already imaged in a prior round.

Supplementary Table 11. Registration error for multiplexed synaptic dataset, measured using the Lectin/SMI/Homer reference channel (**Fig. 5**). S1: mouse #1, S2: mouse #2.

Field of view name	**Round pair**	**# of subvolumes after outlier removal**	**Mean (μm)**	**Lower 95% CI (μm)**	**Upper 95% CI (μm)**
S1ROI1	1-2	1000	0.04259	0.04105	0.04413
S1ROI1	1-3	1000	0.06999	0.06749	0.07248
S1ROI1	1-4	1000	0.0664	0.06432	0.06848
S1ROI1	1-5	1000	0.08332	0.08031	0.08633
S1ROI1	1-6	996	0.07632	0.07346	0.07918
S1ROI1	1-7	999	0.08812	0.08489	0.09135
S1ROI1	1-8	998	0.084	0.08113	0.08688
S1ROI1	1-9	996	0.07642	0.07353	0.0793
S1ROI1	1-10	999	0.08479	0.0814	0.08817
S1ROI1	1-11	994	0.0924	0.08927	0.09554
S1ROI1	1-12	996	0.09051	0.08743	0.0936

S1ROI2	1-2	998	0.04356	0.0424	0.04472
S1ROI2	1-3	1000	0.06717	0.06543	0.06892
S1ROI2	1-4	996	0.06591	0.06407	0.06776
S1ROI2	1-5	997	0.08317	0.08075	0.08559
S1ROI2	1-6	988	0.08298	0.08062	0.08535
S1ROI2	1-7	999	0.08392	0.08144	0.0864
S1ROI2	1-8	987	0.08941	0.08687	0.09194
S1ROI2	1-9	995	0.07788	0.07538	0.08039
S1ROI2	1-10	982	0.1138	0.1096	0.1179
S1ROI2	1-11	987	0.09434	0.09159	0.09709
S1ROI2	1-12	990	0.09294	0.09003	0.09586
S1ROI3	1-2	995	0.02593	0.0247	0.02716
S1ROI3	1-3	985	0.03334	0.03199	0.0347
S1ROI3	1-4	831	0.01928	0.01818	0.02038
S1ROI3	1-5	855	0.02579	0.02457	0.027
S1ROI3	1-6	881	0.0256	0.02423	0.02697
S1ROI3	1-7	974	0.04145	0.03988	0.04303
S1ROI3	1-8	980	0.05178	0.0498	0.05375
S1ROI3	1-9	963	0.05851	0.05692	0.06009
S1ROI3	1-10	968	0.06061	0.05873	0.06249
S1ROI3	1-11	988	0.06048	0.05875	0.0622
S1ROI3	1-12	961	0.0557	0.05388	0.05751
S1ROI4	1-2	998	0.02598	0.02475	0.02721
S1ROI4	1-3	988	0.03342	0.03206	0.03477
S1ROI4	1-4	834	0.01932	0.01821	0.02042
S1ROI4	1-5	858	0.02576	0.02455	0.02697
S1ROI4	1-6	883	0.02561	0.02424	0.02698

S1ROI4	1-7	976	0.04145	0.03988	0.04302
S1ROI4	1-8	982	0.05173	0.04976	0.05371
S1ROI4	1-9	964	0.05854	0.05697	0.06012
S1ROI4	1-10	971	0.06054	0.05867	0.06242
S1ROI4	1-11	991	0.06048	0.05876	0.0622
S1ROI4	1-12	964	0.05569	0.05388	0.0575
S2ROI1	1-2	944	0.0217	0.02087	0.02253
S2ROI1	1-3	996	0.03027	0.02878	0.03175
S2ROI1	1-4	983	0.04392	0.04222	0.04561
S2ROI1	1-5	898	0.02229	0.02118	0.02339
S2ROI1	1-6	863	0.02165	0.02059	0.0227
S2ROI1	1-7	914	0.04288	0.04097	0.04478
S2ROI1	1-8	991	0.05661	0.05446	0.05876
S2ROI1	1-9	858	0.03626	0.03443	0.0381
S2ROI1	1-10	984	0.04589	0.04355	0.04824
S2ROI1	1-11	848	0.02941	0.02806	0.03075
S2ROI1	1-12	985	0.0494	0.04728	0.05151
S2ROI2	1-2	944	0.0217	0.02087	0.02253
S2ROI2	1-3	996	0.03027	0.02878	0.03175
S2ROI2	1-4	983	0.04392	0.04222	0.04561
S2ROI2	1-5	898	0.02229	0.02118	0.02339
S2ROI2	1-6	863	0.02165	0.02059	0.0227
S2ROI2	1-7	914	0.04288	0.04097	0.04478
S2ROI2	1-8	991	0.05661	0.05446	0.05876
S2ROI2	1-9	858	0.03626	0.03443	0.0381
S2ROI2	1-10	984	0.04589	0.04355	0.04824
S2ROI2	1-11	848	0.02941	0.02806	0.03075

S2ROI2	1-12	985	0.0494	0.04728	0.05151
S2ROI3	1-2	1000	0.0452	0.04356	0.04684
S2ROI3	1-3	999	0.04059	0.03893	0.04224
S2ROI3	1-4	1000	0.05878	0.05684	0.06072
S2ROI3	1-5	1000	0.05668	0.05485	0.05851
S2ROI3	1-6	998	0.04476	0.04285	0.04667
S2ROI3	1-7	983	0.05921	0.0567	0.06173
S2ROI3	1-8	994	0.0619	0.05964	0.06416
S2ROI3	1-9	941	0.04499	0.04305	0.04692
S2ROI3	1-10	987	0.0791	0.07618	0.08202
S2ROI3	1-11	987	0.05464	0.05243	0.05686
S2ROI3	1-12	998	0.05848	0.05622	0.06075
S2ROI4	1-2	981	0.02405	0.02309	0.02502
S2ROI4	1-3	999	0.02246	0.02165	0.02328
S2ROI4	1-4	961	0.0238	0.02294	0.02465
S2ROI4	1-5	995	0.02518	0.02396	0.0264
S2ROI4	1-6	971	0.02133	0.02056	0.0221
S2ROI4	1-7	916	0.02806	0.0271	0.02903
S2ROI4	1-8	960	0.0242	0.02319	0.02521
S2ROI4	1-9	961	0.0251	0.02438	0.02582
S2ROI4	1-10	939	0.03724	0.03555	0.03892
S2ROI4	1-11	987	0.02417	0.02301	0.02533
S2ROI4	1-12	974	0.02869	0.02755	0.02984

Supplementary Table 12. Protein and channel information for each round of multiplexed cultured neuron dataset (**Supplementary Fig. 4**).

	ch1 (633)	**ch2 (546)**	**ch3 (488)**

Round 1	SMI/GFAP/Homer/Lectin*	Synapsin 1	NR1
Round 2	SMI/GFAP/Homer	NR2B	SynGAP
Round 3	SMI/GFAP/Homer	GluA1	PSD95
Round 4	SMI/GFAP/Homer	Bassoon	Gephyrin
Round 5	SMI/GFAP/Homer	RIM1	CaMKIIa

*Lectin was excluded from the reference channel in later rounds after negligible immunoreactivity was confirmed, as neuronal cultures are not vascularized.

Supplementary Table 13. Registration error for multiplexed cultured neuron dataset, measured using the SMI/GFAP/Homer reference channel (**Supplementary Fig. 4**).

Field of view name	**Round pair**	**# of subvolumes after outlier removal**	**Mean (μm)**	**Lower 95% CI (μm)**	**Upper 95% CI (μm)**
ROI1	1-2	1000	0.05823	0.05599	0.06047
ROI1	1-3	997	0.05513	0.05297	0.05728
ROI1	1-4	997	0.05094	0.04908	0.0528
ROI1	1-5	934	0.05512	0.05303	0.05721
ROI2	1-2	921	0.03495	0.03392	0.03598
ROI2	1-3	938	0.04504	0.04364	0.04645
ROI2	1-4	961	0.04983	0.04809	0.05156
ROI2	1-5	964	0.03435	0.03304	0.03566
ROI3	1-2	936	0.03399	0.03246	0.03552
ROI3	1-3	999	0.04548	0.04357	0.04739
ROI3	1-4	1000	0.03797	0.03619	0.03975
ROI3	1-5	1000	0.0275	0.02643	0.02858
ROI4	1-2	1000	0.04739	0.04604	0.04874
ROI4	1-3	965	0.05584	0.05409	0.0576

ROI4	1-4	998	0.0594	0.05751	0.06129
ROI4	1-5	1000	0.05947	0.05762	0.06132

Supplementary Table 14. Antibodies that failed with multiExR.

Primary / Secondary	Target	Host	Vendor	Product number	Dilution Factor
Primary	mGluR5	Chicken	Aveslabs	ER5	1:200
Primary	Adam22	Mouse	Antibodies inc	75-093	1:200
Primary	GABA-B	Guinea pig	Millipore Sigma	AB2256	1:200
Primary	CACNA1G	Rabbit	Fisher Scientific	50-173-1816	1:200
Primary	CACNG8	Rabbit	Alamone labs	ACC-125	1:200

Supplementary Table 15. Absolute intensity thresholds used to create binary image volumes for Aβ abundance quantification (**Fig. 3**, see Methods).

Protein	Intensity threshold
D54D2	826
12F4	288
6E10	639

Supplementary Table 16. Absolute intensity thresholds used to create binary image volumes for synaptic protein abundance quantification (**Fig. 3**).

Protein	Intensity threshold
RIM1	259

GluA3	77
NR2B	94
RIM-BP	225
GluA2	40
GluA1	75
NR1	61
Shank3	188
Homer1	479
CaMKIIa	486
Cav2.1	111
GluA4	55
PSD95	379
Bassoon	254
SynGAP	1288
IRSp53	153
Stargazin	71

Supplementary Table 17. List of chemicals

Product Name	Vendor	Product Number
Sodium acrylate	Santa Cruz	CAS7446-81-3
Acrylamide	Sigma	A9099
N,N′-Methylenebisacrylamide (BIS)	Sigma	M7279
Ammonium persulfate (APS)	Sigma	A3678

N,N,N′,N′-Tetramethylethylenediamine (TEMED)	Sigma	T7024
4-Hydroxy-TEMPO (HT)	Sigma	176141
6-((acryloyl)amino)hexanoic Acid, Succinimidyl Ester (AcX)	Thermo Fisher	A20770
Sodium dodecyl sulfate (SDS)	Sigma	436143
Sodium Chloride (NaCl)	Thermo Fisher	AM9760
Tris Buffer, pH 8.0	Fisher scientific	77-86-1
Paraformaldehyde	Electron Microscopy Sciences	15710
Triton X-100	Sigma	X100
Glycine	Sigma	50046
PBS 10x	Thermo Fisher	70011044
Normal Donkey Serum	Jackson ImmunoResearch	017-000-121
Sodium citrate dihydrate	Sigma	W302600

247 **Supplementary Table 18. List of antibodies**

Primary / Secondary	Target	Host	Vendor	Product number	Dilution	Validation
Primary	Cav1.2	Guinea pig	Synaptic Systems	152 205	0.18055556	P[13], VI

Primary	RIM1	Rabbit	Synaptic Systems	140 003	0.18055556	P^{44}, VI, KD
Primary	PSD95	Mouse	Thermo Fisher	MA1-046	0.18055556	P^{230}, VI, KO
Primary	PSD95	Rabbit	Cell Signaling Technology	CST3450S	0.18055556	P^{295}, VI, R
Primary	SynGAP	Rabbit	Thermo Fisher	PA1-046	0.18055556	P^{31}, VI, KO
Primary	Homer1	Rabbit	Synaptic Systems	160 003	0.18055556	P^{141}, VI, KO
Primary	Homer1	Chicken	Synaptic Systems	160 006	0.18055556	P^{22}, VI, KO
Primary	Bassoon	Guinea pig	Synaptic Systems	141 004	0.18055556	No longer in stock*
Primary	Shank3	Guinea pig	Synaptic Systems	162 304	0.18055556	P^{22}, VI, KO
Primary	Gephyrin	Mouse	Synaptic Systems	147 011	0.18055556	P^{206}, VI, KO
Primary	GFAP	Chicken	Abcam	ab4674	0.18055556	P^{522}, VI
Primary	GluA1	Rabbit	Abcam	ab31232	0.18055556	P^{143}, VI, KO, R
Primary	CaMKII	Mouse	Abcam	ab22609	0.18055556	P^{78}, VI
Primary	Synapsin1	Rabbit	Abcam	ab8	0.18055556	P^{52}, VI, R
Primary	NMDAR1	Mouse	ThermoFisher	32-050-0	0.18055556	P^{48}, VI
Primary	VGlut	Rabbit	Synaptic Systems	131 011	0.18055556	P^{187}, VI, KO

Primary	NR2B	Mouse	antibodiesinc	75-101	0.18055556	P^{94}, VI, KO
Primary	GluA4	Rabbit	Cell Signaling Technology	#8070S	0.18055556	P^{15}, VI, R
Primary	GluA2	Mouse	antibodiesinc	75-002	0.18055556	P^{189}, VI, KO
Primary	PLP	Rabbit	Abcam	ab28486	0.18055556	P^{78}, VI
Primary	Stargazin	Mouse	ThermoFisher	PIMA527645	0.18055556	VI
Primary	Stargazin	Rabbit	Cell Signaling Technology	#8511	0.18055556	P^{5}, VI, R
Primary	GluA3	Mouse	ThermoFisher	32-040-0	0.18055556	P^{8}, VI, KO
Primary	GluA3	Rabbit	Abcam	ab40845	0.18055556	P^{19}, VI
Primary	RIM-BP	Rabbit	Synaptic Systems	316 103	0.18055556	P^{9}, VI, KO
Primary	Aβ42 (6E10)	Mouse	BioLegend	SIG39320	0.18055556	P^{331}, VI
Primary	Aβ42 (12F4)	Mouse	BioLegend	SIG39142	0.18055556	P^{31}, VI
Primary	Aβ42 (D54D2)	Rabbit	Cell Signaling Technology	CST8243S	0.18055556	P^{116}, VI, R
Primary	SMI	Chicken	Abcam	ab4680	0.31944444	P^{118}, VI, R
Primary	SMI	Chicken	BioLegend	822601	0.18055556	P^{9}, VI
Primary	Kv7.2	Mouse	Santa Cruz	sc-271852	0.18055556	P^{7}, VI, R
Primary	Nav1.6	Rabbit	Abcam	ab65166	0.18055556	P^{9}, VI, R
Primary	Erbb4	Rabbit	Cell Signaling Technology	CST4795	0.18055556	P^{81}, VI
Primary	Elfn1	Rabbit	Synaptic Systems	448 003	0.18055556	P^{2}, VI, KO

Secondary	Mouse	Goat	ThermoFisher	A28175 (Alexa Fluor 488 nm)	1:200	N/A
Secondary	Mouse	Goat	ThermoFisher	A11031 (Alexa Fluor 546 nm)	1:200	N/A
Secondary	Mouse	Donkey	Biotium	20124 (CF 633 nm)	1:200	N/A
Secondary	Mouse	Donkey	ThermoFisher	A10036 (Alexa Fluor 546 nm)	1:200	N/A
Secondary	Rabbit	Goat	ThermoFisher	A11034 (Alexa Fluor 488 nm)	1:200	N/A
Secondary	Rabbit	Goat	ThermoFisher	A11035 (Alexa Fluor 546 nm)	1:200	N/A
Secondary	Rabbit	Donkey	Biotium	20125 (CF 633 nm)	1:200	N/A
Secondary	Rabbit	Donkey	ThermoFisher	A10040 (Alexa Fluor 546 nm)	1:200	N/A
Secondary	Guinea pig	Donkey	Biotium	20171 (CF 633 nm)	1:200	N/A
Secondary	Chicken	Goat	ThermoFisher	A11039 (Alexa Fluor 488 nm)	1:200	N/A
Secondary	Chicken	Donkey	Biotium	20168 (CF 633 nm)	1:200	N/A

P: publications, number of references in superscript, VI: vendor image(s), KO: knock-out, KD: knock-down, R: high user rating (4 or more stars out of 5).
*Its replacement, Synaptic Systems 141 318 is supported by KO, P, and VI.

Supplementary Table 19. Gel solution of ExR

Monomer solution:

Component	**Stock Concentration***	**Amount (mL)**
Sodium acrylate	33% (w/w)*	9
Acrylamide	50% (w/w)*	2
Sodium Chloride	5 M	16
PBS	10x	4
Water	-	3.6
Total	-	34.6

*As weight/weight. For instance, 10 g sodium acrylate powder was dissolved in 20 mL deionized water as 33% (w/w) stock solution. 10 g acrylamide powder was dissolved in 10 mL deionized water as 50% (w/w) stock solution.

Gelling solution:

Reagent	**Stock Concentration**	**1st gel solution (µL)**	**Re-embedding solution (µL)**	**3rd gel solution (µL)**	**Additional re-embedding solution (µL)**
Monomer	-	864	-	864	-
Acrylamide	50% w/w	-	275	-	40
Bis acrylamide	1.96% w/w	40	18.75	20	18.75
Water	-	36	701.25	111	936.25
4HT	0.50% w/w	20	-	-	-
TEMED	8% w/w	20	2.5	2.5	2.5
APS	9.10% w/w	20	2.5	2.5	2.5
Total (mL)	-	1	1	1	1

Denaturation buffer:

Reagent	**Stock Concentration**	**Amount (mL)**

Sodium dodecyl sulfate (SDS)	700 mM	11.43
Water	-	24.97
Tris buffer, pH 8.0	1 M	2
Sodium Chloride	5 M	1.6
Total	-	40

260

Supplementary Note 1

We take the mean of all pixels in the image weighted by their similarity to the target pixel. Consider an image having an area Ω and points (p, q) in the image. The filtered values at a point p is

$$u(p) = \frac{1}{C(p)} \int_{\Omega} v(q) f(p,q) dq \quad \forall\, q \in \Omega$$

Here $f(p,q)$ is the weighting function of choice and $C(p)$ is the normalization factor.

$$C(p) = \int_{\Omega} f(p,q)\, dq$$

In our case, we choose $f(p,q)$ to be a Gaussian weighting function

$$f(p,q) = e^{-\frac{|B(q) - B(p)|^2}{h^2}}$$

Whose standard deviation is h which serves as the filtering parameter, and $B(\cdot)$ is the local mean of an image point.

Supplementary Note 2

Since images obtained from expansion sequencing have inhomogenous lighting, we propose to make use of local (or adaptive thresholding) where we define a threshold T for neighboring regions of a pixel at location (i, j).

Within this neighborhood, we replace pixels with a binary mask subject to intensity $I_{i,j}$subject to the following piecewise condition:

$$f(i,j) = 0 \quad T > I_{i,j}$$

$$255 \quad T < I_{i,j}$$

Supplementary Note 3

Given two corresponding point sets $X = \{x_1, \cdots, x_n\}$ and $P = \{p_1, \cdots, p_n\}$, we wish to obtain a rotation R and a translation t such that the mean squared error

$$E(r,t) = \frac{1}{N} \sum_{i=1}^{N} ||x_i - Rp_i - t||^2$$

is minimized. For generating the correct correspondences, we propose a heuristic approximation where the nearest neighbors in the point cloud represent corresponding synapses. The closest alignment is found iteratively and is said to converge if the error in spatial alignment of both clouds is within a specified tolerance value t_0.

Supplementary Note 4

More often than not, synapse point clouds of the fixed and moving image volumes are deformed by a non-rigid transformation. Generally, these points do not lie on a structured grid. This encourages the use of interpolants obtained from Radial Basis Functions (RBFs).

Thin-plate splines themselves a natural representation in the form of RBFs. For a set of control points $\{c_i, i = 1,2, \cdots, K\}$ a spatial mapping is defined from an arbitrary location x to a new location $f(x)$.

$$f(x) = \sum_{i=1}^{K} w_i\, \varphi(||x - c_i||)$$

294 $||\cdot||$ denoting the $L2$-norm of the vectors and $\{w_i\}$ is a set of mapping coefficients. The thin plate spline
295 corresponds to the kernel given by

296 $$\varphi(r) = r^2 \log r$$

297

Supplementary References

1. Seabold, S. & Perktold, J. Statsmodels: Econometric and Statistical Modeling with Python. *PROC. 9th PYTHON Sci. CONF* (2010).